Middle East Journal of Science

www.dergipark.org.tr/mejs

MEJS

VOLUME 9
ISSUE 2

DECEMBER 2023

E-ISSN 2618-6136

Email : bilgumus@gmail.com
Visit our home page on www.dergipark.org.tr/mejs

Field: Biological Sciences
(Assoc.Prof.Dr., Department of Plant Physiology and Biotechnology, Research Institute of Crop Husbandry, Ministry of Agriculture of the Republic of Azerbaijan)
tamraz.tamrazov@mail.ru

Yusuf ZEREN

Field: Mathematics, Topology

(Assoc.Prof.Dr., Yıldız Technical University, Faculty of Science and Letters, Dep. of Mathematics, TURKEY)

yzeren@yildiz.edu.tr

Z. Gökay KAYNAK

Field: Nuclear Physics

(Retired Prof.Dr., Uludag University, Faculty of Science, Dep. of Physics, Turkey) kaynak@uludag.edu.tr

Middle East Journal of Science

https://dergipark.org.tr/mejs

e-ISSN:2618-6136

MEJS
Volume 9
Issue 2
December 2023

CONTENTS

Research Articles

Middle East Journal of Science

https://dergipark.org.tr/mejs **MEJS**

e-ISSN:2618-6136

Research Article

INVESTIGATION OF CENTERING PROBLEM IN THE CADMIUM ZINC TELLURIDE (CZT) CARDIAC CAMERA

***Eda MUTLU*[1,2], *Bilal KOVAN*[3], *Emine Göknur IŞIK*[3], *Bayram DEMİR**[4], *Serkan KUYUMCU*[3]**

[1]Istanbul University, Institute of Graduate Studies in Sciences, Nuclear Physics, İstanbul, Türkiye
2Altinbas University, Vocational School Health Services, Radiotherapy Program, İstanbul, Türkiye
3Istanbul University, Istanbul Faculty of Medicine, Department of Nuclear Medicine, İstanbul, Türkiye
4Istanbul University, Science Faculty, Physics Department, İstanbul, Türkiye
* Corresponding author; baybay@istanbul.edu.tr

Abstract: *Cadmium Zinc Telluride (CZT) Cardiac Cameras are a special SPECT cameras with solid state cadmium zinc telluride detectors. This diagnostic method applied in the evaluation of coronary artery disease is well designed for myocardial perfusion scintigraphy. Aim: CZT cardiac cameras have a limited detector area. In patients who are morbidly obese or whose heart is not in its normal location in the body, the center of the heart and the isocenter of the device do not coincide. It is aimed to investigate how these conditions affect the imaging performance of the CZT cardiac camera. A homogeneous and spherical ball with a diameter of 4 cm was used for the research. To be able to measure away from the center a wooden phantom with 8 cavities and a total length of 32 cm was designed. The center as reference point has been determined by matching the center of the device with the center of the sphere. For the next imaging, the image was taken by placing the spherical ball in the other cavities, respectively, without changing the center. According to the results obtained, farther from the center, deviations from sphericity and differences in dose distribution were observed. Counts decreased by 1.5% in the 2nd position and 16% in the 3rd position relative to the center in the X-axis. A disaster area has been formed and the image area has been exited from the 4th imaging. It is very important to center the patient as much as possible, otherwise the doctor will misdiagnose.*

Keywords: *Cardiac Imaging, (CZT) SPECT, Nuclear Medicine, Centering Problem.*

Received: March 23, 2023 *Accepted: July 25, 2023*

1. Introduction

Nuclear medicine is a branch of science in which diagnostic imaging and treatments are performed with the help of radionuclides given to the body. Radionuclides affect the biochemical and physiological processes of the human body, and the radiation emitted during their disintegration during the steady state is detected by detectors. The detection of radiations emitted by radioactive materials is provided by Single Photon Emission Tomography (SPECT) and Positron Emission Tomography (PET).

Development of the technology of devices used in nuclear medicine imaging; made significant contributions in terms of image quality, imaging time, and patient radiation dose. Studies in SPECT systems in recent years aim to increase system efficiency and image resolution [1]. One of these devices is the new generation of Cadmium Zinc Telluride (CZT) Cardiac Cameras, developed with this goal and started to be used in nuclear cardiology [2-3].

CZT Cardiac Cameras are specialized SPECT cameras with solid state cadmium zinc telluride detectors. It is designed for myocardial perfusion scintigraphy, most commonly used in nuclear cardiac

studies. Myocardial perfusion imaging (MPI); it is an examination based on imaging the distribution of blood flow feeding the myocardium by means of an intravenous (IV) radiopharmaceutical. It is a two-stage physiological event; first, the radiopharmaceutical must be able to go to the myocardial tissue, and second, metabolically active myocardial cells must be able to capture this substance. MPI; it is used to identify areas of a patient with relative or absolute decreased myocardial agent associated with coronary artery disease, infarction, ischemia, or scarring [4-6].

Cardiac imaging is a frequently used diagnostic method in obese and morbidly obese individuals. Obesity; it is a risk factor for cardiovascular diseases such as hypertension, coronary artery disease, heart failure and atrial fibrillation. Therefore, cardiac imaging evaluation is very necessary in obese patients. More soft tissue attenuation in obese patients reduces the accuracy of MPI. Research proves that with CZT detectors, the artifacts of SPECT can be reduced and image quality improved. [7]. However, the device's limited detector area is not suitable for patients who are morbidly obese or whose heart is not in its normal position in the body. In these patients, the center of the heart and the isocenter of the device do not coincide. This creates the centering problem. The aim of the present study is to create a centering problem using a phantom in a CZT cardiac camera and to investigate the effect of images obtained outside of centering on image quality.

2. Materials and Methods

2.1. CZT Gamma Camera

It is an alternative detection system to conventional gamma cameras for gamma ray detection and imaging in nuclear medicine. Radiation detection efficiency is high as the solid material in its structure effectively blocks the gamma rays. Unlike conventional gamma cameras with standard [NaI(Tl)] crystals, the CZT detector is a semiconductor with higher count sensitivity that directly converts gamma photon energy into an electrical signal. The device has a C-shaped gantry containing multiple detectors (Fig. 1). It has 19 fixed detectors arranged in 3 rows, oriented perpendicular to the long axis of the patient, each equipped with multipinhole collimators with an aperture diameter of 5.1 mm. Nine detectors are positioned along a transaxial portion and are dispersed around 180°. Other detectors are tilted and positioned in two groups of five detectors on either side of the main detector row. All detectors view the same center of rotation where the heart should be positioned [8-9]. In Figure 2, the center of the CZT detectors and the positions of the balls during imaging to create a centering problem are shown.

2.2. Phantom

A homogeneous and spherical ball with a diameter of 4 cm was used for the research. To be able to measure away from the center; measurements were taken at 4 cm intervals along the X-axis and Z-axis. On the diagonal, measurements were taken at 4x1.41 = 5.6 cm intervals (Fig. 2). There are no spaces between the cavities. A wooden phantom with 8 cavities and a total length of 32 cm was designed. In order to place the spheres on the phantom, the diameter of the cavities in the phantom is equivalent to the diameter of the spherical ball. Tc-99m was used in myocardial perfusion scintigraphy. Tc-99m activity was measured in the Atomlab 500 dose calibrator for injection into the spherical ball.

Figure 1. Cadmium Zinc Telluride (CZT) Cardiac Camera.

2.3. Measurements

5 mCi Tc-99m activity was added into a 0.5 lt water-filled pet bottle and it was shaken for 1 minute and distributed homogeneously. Then the homogeneous mixture was injected into the spherical ball. For the first imaging, the spherical ball was placed in the first recess of the phantom. By matching the center of the device with the center of the sphere; the center, which is our reference point, has been determined. For the next imaging, the image was taken by placing the spherical ball in the other cavities, respectively, without changing the center. A total of 8 images were obtained by moving the spherical ball 4 cm away from the center along the X-axis. A total of 5 images were taken by moving the spherical ball 4 cm away from the center along the Z-axis. A total of 5 images were obtained by moving the spherical ball 5.6 cm from the center along the diagonal axis. Figure 3.a shows the centered imaging where the isocenter of the device and the center of the active sphere coincide, X-1; it represents the active sphere imaging placed in the first slot in an 8-slot board. In Figure 3.b, it is shown how the imaging takes place at a distance of 4 cm from the center (X-2), and in Figure 3.c, at a distance of 12 cm from the center. Images were obtained by placing the active sphere in the 2nd cavity for X-2 imaging, and the active sphere in the 4th cavity for X-4 imaging. Continuing in the same way, imaging in all axes was completed.

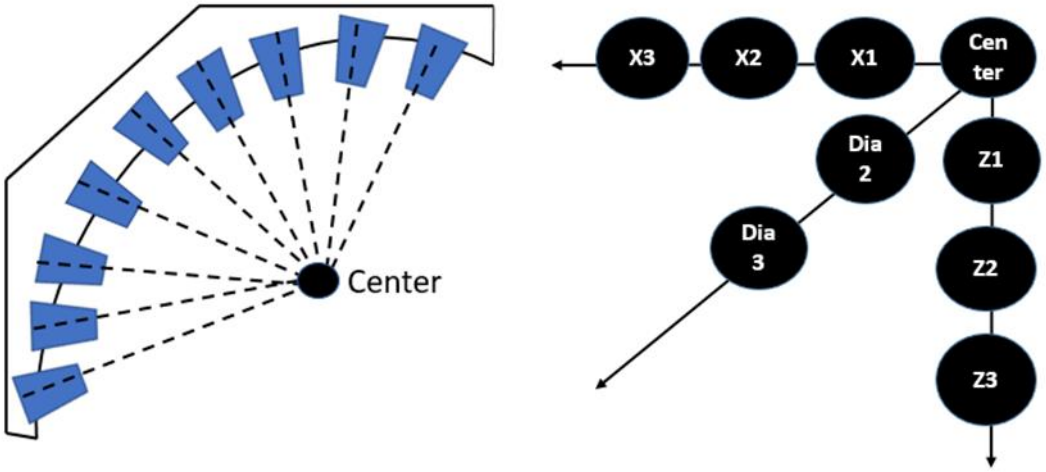

Figure 2. The center of CZT detectors (left), The positions of the balls during imaging to create a centering problem (right).

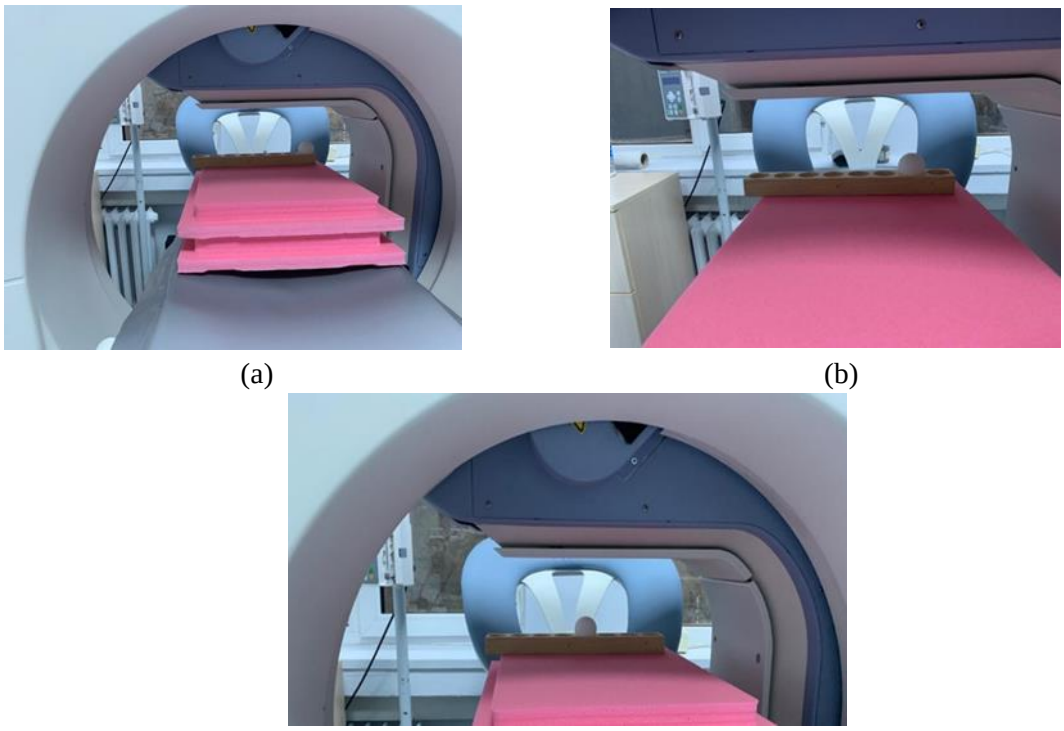

(a) (b)

(c)

Figure 3. a.) Centered imaging X-1, b.) Example of imaging (off-centre imaging), X-2, c.) Example of imaging (off-centre imaging), X-4.

3. Results and Discussion

In CZT cardiac cameras, whose gantry is smaller than conventional cameras, heart focused collimation is performed by using multipinhole collimators. In the geometry where the multipinhole collimators are fixed and focused on the concentric of the device, the center of the collimators and the

center of the heart are overlapped to obtain images with focused imaging capability optimized for the heart. The geometry of the device allows simultaneous detection of counts from all directions without rotating the detectors. The device has high energy resolution and spatial resolution [10]. Due to the high energy resolution, the energy window can be narrower, thus reducing scattering. High quality images are obtained with high spatial resolution. All these innovations significantly reduce imaging time and expose the patient to less radiation compared to conventional SPECT.

While providing positive results supported by studies in the literature for normal patient using CZT cardiac cameras, these results may differ for obese patients. The quality of images obtained in nuclear medicine imaging is of great importance for the correct diagnosis of patients. CZT imaging can be performed in patients with normal weight (BMI: 18.5-24.9 kg/m^2) and overweight (BMI: 25-29.9kg/m^2). But, in obese (BMI: 30-40 kg/m^2) and morbidly obese (BMI $\geq$ 40 kg/m^2) patients, it cannot be performed correctly because the detector cannot get close enough to the patient due to the limited detector area.

In a study comparing conventional SPECT and CZT-SPECT for myocardial perfusion imaging, the total radiation doses received by the patients matched according to gender, age and body mass index were compared. While it was determined that the patients received lower radiation doses in the imaging performed with CZT-SPECT, it was observed that the obese patients among the comparison patients received a higher radiation dose than the normal-weight patients [11].

In the study of Michael et al. [12], image quality analysis was performed for 63 patients in a similar study in which myocardial perfusion scintigraphy was evaluated in CZT SPECT in patients with high, very high, and excessive body mass index. The image quality assessment was based on predefined cardiac image features and radioactivity uptake. SPECT images of the same patients were also evaluated for comparison. According to the results obtained, it was concluded that SPECT should be planned because it is difficult to obtain diagnostic image quality in CZT in patients with a body mass index of 40 kg/m^2 and above. The present study is a phantom study, and it allows the evaluation of image quality by including count and volume information according to the distance from the center. Our results also show parallels to the results of Michael et al. Since there is a possibility that the hearts of patients with a BMI index above 40 kg/m^2 may go out of the Field of View (FOV) of the CZT cardiac cameras, it is recommended that these patients be included in SPECT.

The spherical ball used in the present study has a volume of 33.4 cm^3. While obtaining the image of the spherical ball in the center, the threshold value corresponding to 33.4 cm^3 volume was determined. This value is 24%. While obtaining data from other images, a threshold was determined as 24% and all results were obtained using this value. When the results are evaluated; for all 3 plans, count values decreased as they moved away from the center and deviations from sphericity were observed. This variation is more pronounced in the X and diagonal axis measurements, as we expected. Counts decreased by 1.5% in the 2nd position and 16% in the 3rd position compared to the center in the X-axis. Counts decreased by 3.9% in the 2nd position and 21.7% in the 3rd position compared to the center in the diagonal axis. Counts decreased by 9.9% in the 2nd position and 11.9% in the 3rd position compared to the center in the Z-axis. For each axis, a disaster area was formed from the 4th image. Thus, the imaging was stopped and the image area was moved out. The results obtained were evaluated in the axial, coronal, and sagittal planes. And results are given in Fig. 4, Fig. 5, and Fig. 6.

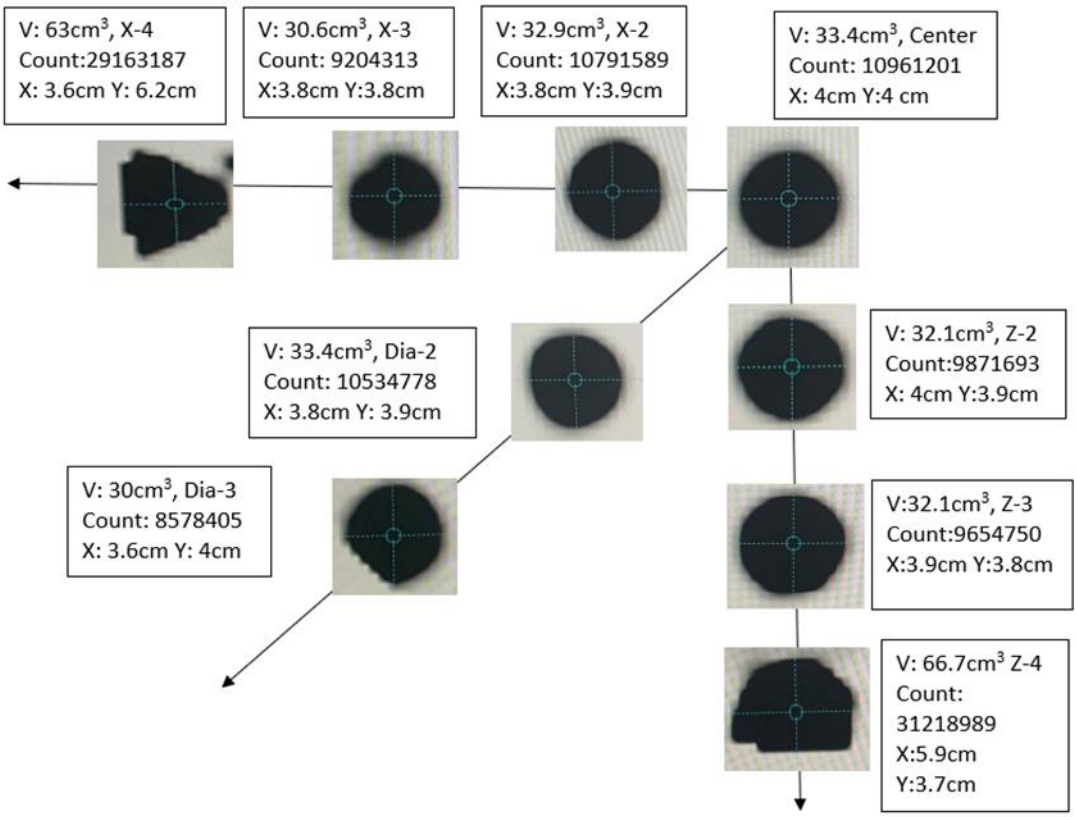

Figure 4. Images taken in axial plane and measurement results.

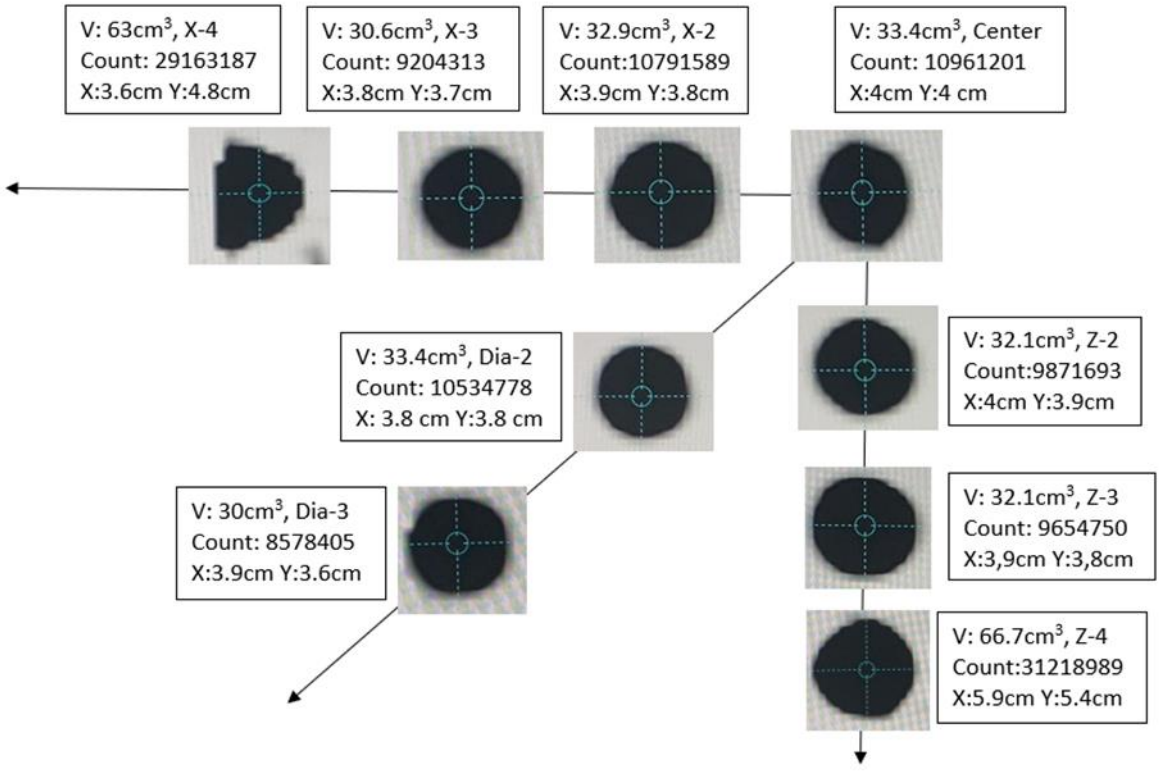

Figure 5. Images taken in the coronal plane and measurement results.

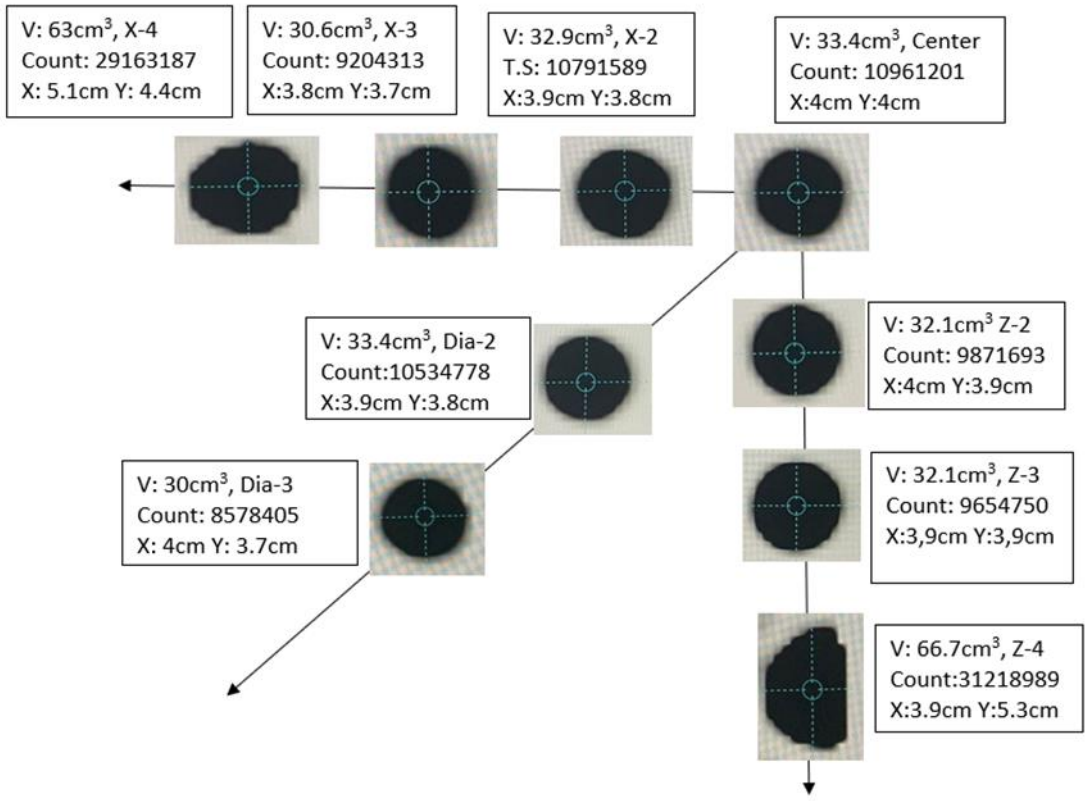

Figure 6. Images taken in the sagittal plane and measurement results.

If we clinically evaluate the count loss in imaging from outside the center; myocardial ischemia can be interpreted as infarction. This causes an incorrect perfusion defect. As there is a change in the dimensions of the sphere as it moves away from the center for all axes, the total volume also changes. Compared to the 3rd imaging made on the central volume axes; It decreased 8.4% for the X-axis, 3.9% for the Z-axis and 10.2% for the diagonal axis.

In a similar study in which MPI imaging was performed on CZT camera in 18 patients; after first obtaining an image with the heart positioned in the center of the quality field of view (QFOV), the patients were re-imaged at different positions 5-20 mm from the center. Examined positions; moving the camera 5, 10 and 20 mm away from the patient, lowering the table 20 mm and moving the table inward 20 mm. When the acquired images were evaluated, a count loss was observed for all off-center images tested, as in our study [13]. The study provides information on images up to 2 cm off center. Considering the patients with a limited 18 cm area of the FOV field and where centering cannot be performed, it is important to know how far off-center the image is obtained and what the results are. The present study provides information on images from 8 cm from the center for the X and Z axes and 11.2 cm from the center for the diagonal axis.

For centered and off-center imaging along the X axis, the variation in counts of the spheres along the diameter was investigated. Dose profiles were given in Fig. 7, Fig. 8 and Fig. 9. As shown in Figures 7, 8, and 9, when we look at the change in count along the diameter of the spherical ball according to the distance from the center, the count difference increases as the distance from the center increases and the homogeneity deteriorates. When we compare the count reductions in the centers of the spherical balls, they decreased by 31.8% for X-1 imaging, 34.8% for X-2 imaging and 47.85% for X-3 imaging. This is due to decreased counting efficiency and self attenuation of balls. While less collapse is observed in the center compared to the edges in X-1 imaging, collapse is more in X-2 and X-3 imaging. This

effect is significant as attenuation correction is not performed using CT on the CZT cardiac camera device. Especially if imaging is done for X-3 position and after, a uniform distribution may appear quite distorted. This causes misinterpretation.

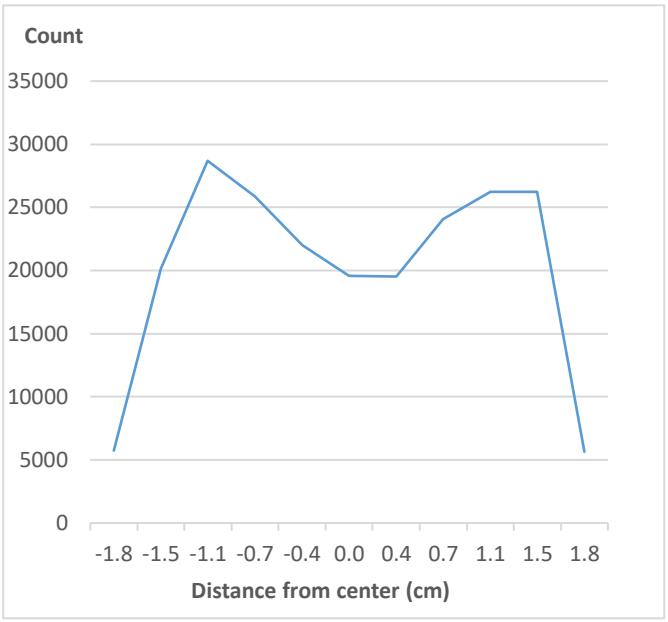

Figure 7. Count variation along the diameter of the centered sphere, X-1.

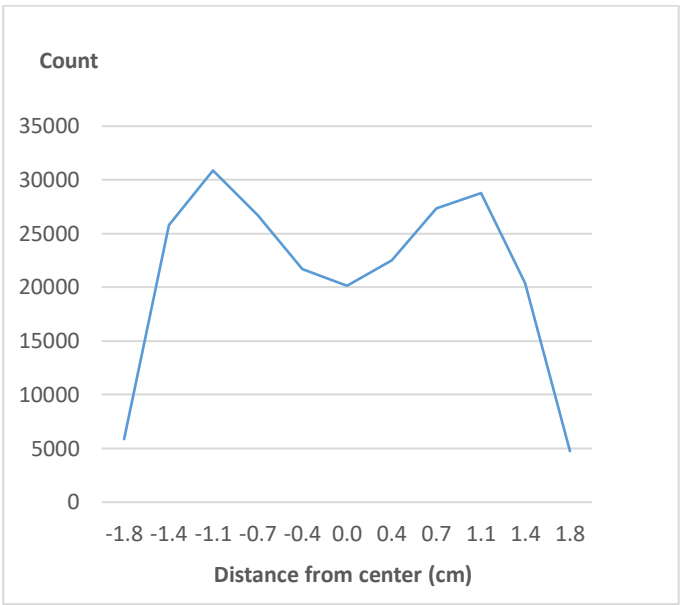

Figure 8. Count variation along the diameter of the sphere 4 cm from the center, X-2.

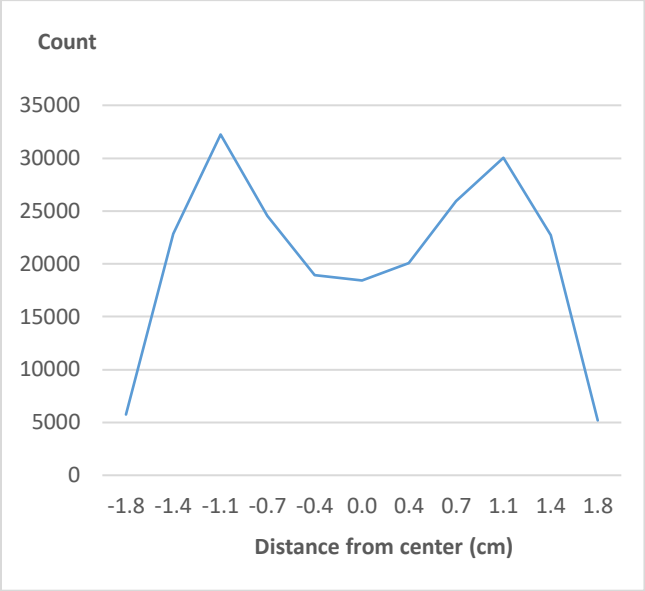

Figure 9. Count variation along the diameter of the sphere 8 cm from the center, X-3.

4. Conclusion

According to the phantom results obtained from a 4 cm diameter ball filled Tc-99m; the farther from the center of the ball, the counting efficiency decreases, the shape changes (such as narrowing or widening of the axes, decrease in the volume) and deterioration of the homogeneous distribution have emerged. Interpretation of images obtained in this way may lead to misdiagnosis and thus affect the patient's treatment. It is of utmost importance to always ensure optimal patient positioning. Since centering cannot be performed in patients who are morbidly obese, have a wide chest wall and large breast structure, and whose hearts are not in their normal positions in the body, it is recommended to perform heart extractions using a conventional SPECT device.

Ethical Statement:

Our study does not cause any harm to the environment and does not involve the use of animal or human subjects. Therefore, it was not necessary to obtain an Ethics Committee Report.

Conflict of İnterest:

The authors must notify of any conflicts of interest.

Authors' Contributions:

E.M: Writing - Original Draft Preparation, Investigation, Conceptualization, Data Collection and Processing, Resources (%40).
B.K: Formal Analysis, Methodology, Resources (%20).
E.I: Methodology, Critical Review (%10).
B.D: Formal Analysis, Methodology, Critical Review, Comment (%20).
S.K: Critical Review, Comment (%10).
All authors read and approved the final manuscript.

References

[1] Ben-Haim, S., Kennedy, J., Keidar. Z., "Novel Cadmium Zinc Telluride Devices for Myocardial Perfusion Imaging-Technological Aspects and Clinical Applications", *Seminars in Nuclear Medicine*, 46(4):273-85, 2016.

[2] Baumgarten, R., et al., "Radiation exposure after myocardial perfusion imaging with Cadmium-Zinc-Telluride camera versus conventional camera*", J Nucl Cardiol.*, 28(3):992-999, 2020.

[3] Henzlova M.J., Duvall L., "Is the CZT technology the future of nuclear cardiology?" *Journal of Nuclear Cardiology*, 29:737–740, 2020.

[4] Duncker, D.J., Koller, A., Merkus, D., Cantry Jr J.M., "Regulation of coronary blood flow in health and ischemic heart disease", *Progress in Cardiovascular Diseases*, 57(5):409-422, 2015.

[5] Agostini, D., et al., "Performance of cardiac cadmium-zinc-telluride gamma camera imaging in coronary artery disease: a review from the cardiovascular committee of the European Association of Nuclear Medicine (EANM)", *Eur J Nucl Med Mol Imaging*, 43(13):2423-2432, 2016.

[6] Zhang, Y.Q., et al. "Diagnostic value of cadmium-zinc-telluride myocardial perfusion imaging versus coronary angiography in coronary artery disease: A PRISMA-compliant meta-analysis", *Medicine (Baltimore)*, 98(9): e14716, 2019.

[7] Zhang H., et al., "Left ventricular mechanical dyssynchrony assessment in obese patients using the cadmium-zinc telluride SPECT camera", *The International Journal of Cardiovascular Imaging*, 36(4):757–765, 2020.

[8] Ljungberg M., Pretorius H., "SPECT/CT: an update on technological developments and clinical applications", *British Institute of Radiology*, 91(1081):20160402, 2018.

[9] Buechel, R.R., et al., "Ultrafast nuclear myocardial perfusion imaging on a new gamma camera with semiconductor detector technique: First clinical validation", *Eur J Nucl Med Mol Imaging*, 37(4):773-778, 2010.

[10] Kincl, V., Drozdova, A., Vasina, J., Panovsky, R., Kaminek, M., "Cadmium–zinc–telluride SPECT scanners – New perspectives in nuclear cardiology", *Cor et Vasa*, 57(3): e214-e218, 2015.

[11] Budzyńska, A., Osiecki, S., Mazurek, A., Piszczek, S., Dziuk, M., "Feasibility of myocardial perfusion imaging studies in morbidly obese patients with a cadmium-zinc-telluride cardiac camera", *Nucl Med Rev Cent East Eur.*, 22(1):18-22, 2019.

[12] Fiechter, M., et al., "Cadmium-Zinc-Telluride Myocardial Perfusion Imaging in Obese Patients", *The Journal Of Nuclear Medicine*, 53(9):1401-6, 2012.

[13] Hindorf, C., Oddstig, J., et al., "Importance of correct patient positioning in myocardial perfusion SPECT when using a CZT camera", *Journal of Nuclear Cardiology*, 21(4):695-702, 2014.

Middle East Journal of Science

https://dergipark.org.tr/mejs **MEJS**

e-ISSN:2618-6136

Research Article

SIMULATION STUDIES OF Cr-doped CuO HETEROJUNCTION SOLAR CELLS

***Serap YIGIT GEZGIN*[1] *Silan BATURAY**[2] *Ilhan CANDAN*[2] *Hamdi Sukur KILIC*[1,3,4]

[1]Department of Physics, Faculty of Science, University of Selcuk, 42031 Selcuklu, Konya, Turkiye
[2]Department of Physics, Faculty of Science, Dicle University, 21280 Diyarbakir, Turkiye
[3]Direc. of High Technology Research and App. Center, University of Selcuk, 42031 Selcuklu, Konya, Turkiye
[4]Direc. of Laser-Induced Proton Therapy App. and Res. Center, University of Selçuk, 42031 Konya, Turkiye
*Corresponding author: silan@dicle.edu.tr

Abstract: *1% and 3% Cr-doped CuO thin films have been deposited on soda lime glass by the spin coating method, and then their structural, topological, and optical properties have been studied by operating X-ray diffraction, scanning electron microscopy and Ultraviolet-Visible spectroscopy techniques, respectively. XRD patterns of CuO: Cr (1%) and CuO: Cr (3%) thin films demonstrate characteristics of monoclinic CuO structure with a C2/c space group. The morphology of coated film plays an important role in analyzing some optoelectronic properties. 1% Cr-doped CuO thin film absorbs more photons compared to 3% Cr-doped CuO in Vis and UV regions. The band gaps of 1% Cr and 3% Cr-doped CuO thin films are to be 2.18 eV and 2.30 eV, respectively. The Mo/Cr: CuO/SnO_2/n-ZnO/i-ZnO/AZO solar cells have been modeled with the SCAPS-1D simulation program. The photovoltaic parameters of solar cells deteriorated with some increase in the neutral defect density value. As the shallow acceptor defect density value is increased, short-circuit current density (J_{SC}) is decreased, short-circuit current density (V_{OC}), fill factor (FF) and efficiency (η) are increased. The photovoltaic parameters' performance of 1% Cr-doped CuO solar cells was found to be better than that of 3% Cr-doped CuO solar cells. The efficiency of 1% Cr-doped CuO solar cells is increased with the use of a SnO_2 intermediate layer in 2 nm thickness at the heterojunction interface.*

Keywords*: Cr-doped CuO, thin film, solar cells, SCAPS-1D*

Received: April 28, 2023 *Accepted: December 4, 2023*

1. Introduction

The *p*-type copper oxide (CuO) semiconductor has gained much attention in recent years. As a matter of fact, it has presented some attractions in a fundamental way in various areas of science such as chemistry, physics, and material science. Due to being a non-toxic, inexpensive, and easily found raw copper material, CuO is a promising compound [1]. CuO has a monoclinic structure and small optical band gap that varies between 1.56 eV and 2.46 eV [2]. CuO is an exclusive monoxide material for significant surveys as well as many practical applications such as photocatalysis [3, 4], lithium batteries [5], high-Tc superconductor [6-8], gas sensors [9-11], magnetic storage [12], and solar cell applications [13, 14]. Copper oxide has been produced employing numerous methods, including reflux condensation [15, 16], chemical bath deposition [2], sol-gel [17, 18], radio frequency plasma-aided pulsed laser [19], thermal oxidation [20], electrodeposition [21], reactive DC magnetron sputtering [22], evaporation of simple solvent [23] solution casting [24], and spray pyrolysis [25]. The spin coating technique is a deposition procedure that has attracted the research community's significant attention. It has numerous advantages, such as low-cost technique, simplicity, adherent production, effectiveness reproducibility,

stoichiometry, and homogenous deposition of thin films. Furthermore, it does not need a vacuum or sophisticated materials, thus it is very easy to work with. The resistivity of CuO is quite high, and not many studies have been carried out to investigate the nature of substrate influence, which is an important parameter which reduces the resistivity layer. Therefore, layers of CuO/ glass and CuO/SnO_2:F/glass were studied to reveal the impact of substrate nature on CuO thin films' physical characteristics, particularly the investigation of properties related to photovoltaic (PV) applications.

There can be negative factors such as lattice mismatch, interface states, defects and traps, and mismatched band alignment between *p*- and *n*-type semiconductors in a heterojunction solar cell. The SnO_2 intermediate layer can be used to passivate interfacial defects. SnO_2 allows electron transfer while preventing the transition from the absorber layer to the buffer layer. This allows charge collection and increased efficiency in a solar cells [26].

Zinc oxide (ZnO) samples are a binary semiconductor material that have been extensively studied recently due to their excellent electrical, optical, and magnetic properties. They are also highly transparent, have a wide energy band gap value, and are nontoxic. These properties have led to extensive research [27-30]. ZnO thin films typically display *n*-type conduction at Zn rich conditions. It was happened by a deviation from stoichiometry due to 'intrinsic' donors including, oxygen vacancies, H incorporation, and zinc interstitials [29]. On the additional hand, the *p*-type conduction in zinc oxide is usually stated by relatively low hole-mobility and low hole-concentration as well as instability due to the deep acceptor-levels of the dopant element.

Recently, a simulation program employed to determine the solar cell' efficiency with the use of layers that form solar cell has gained significant. One of the most commonly employed programs in this area is SCAPS-1D (one-dimensional simulation software) that calculates a solar cell's PV parameters by parameters including energy band gap, dielectric permittivity, thin film thickness, the layers' electron affinity when constructing the solar cells, the contact material's work function [31, 32]. It was generated at the University of Gent in the Electronics and Information Systems' Department. Depending on Auger electron/hole capture coefficient, interfacial defect density, and operation temperature parameters [33], solar cells' PV parameters can be calculated, and hence, a reliable forecast could be done on the solar cell's performance.

Doping has a large impact on the structural, electrical and optical properties of CuO film. However, a few experimental studies have available on the experimental and photovoltaic calculation for solar cells. Thus, to get more light in understanding of the effect of doping ratio and back contact on physical properties of Cr:CuO film, more experimental and theoretically studies are necessary. We have studied the influences of Cr doping on the structural, topological, optical, and photovoltaic properties of CuO film. In this study, 1% and 3% Cr-doped CuO thin films were fabricated by a system of spin coating. 1% and 3% Cr-doped CuO thin films' structural, topological, and optical properties were examined by X-ray diffraction (XRD), scanning electron microscopy (SEM), and Ultraviolet-Visible spectrophotometry (UV-Vis), respectively. Moreover, by employing SCAPS simulation program, the solar cells consisting of Mo/Cr:CuO/SnO_2/*n*-ZnO/i-ZnO/AZO layers were modelled.

2. Materials and Methods

Analytical-grade precursor copper (II) acetate ($Cu(CH_3COO)_2.H_2O$, 0.1 M) and chromium (III) chloride ($CrCl_3.6H_2O$, 0.01 M) were used in this study. Sufficient $CrCl_3.6H_2O$ was mixed in the $Cu(CH_3COO)_2.H_2O$ to obtain doping concentrations of 1 and 3 at.%, and the liquid dark blue solutions were stirred for 5 h at room temperature. Ethanol and diethanolamine (1:10) were used throughout the experimental procedures as solvents and stabilizers, respectively. Before the coating fabrication process, SLG substrates were firstly boiled in a 5:1:1 deionized water (H_2O), ammonia, and hydrogen peroxide (H_2O_2) mix for a time of around 20 min. at a temperature of ~90 ^{O}C and in a solution of the same ratio

of H_2O, H_2O_2, and hydrogen chloride at the same temperature and time to remove the unnecessary impurities on the SLG substrate [18]. The obtained solutions were deposited on SLG substrates to obtain 1 and 3% Cr-doped CuO films by spin coating method at 1500 rpm for 55 s. After this, the coating thin films were annealed for around 60 min in a furnace at ~500 ^{O}C. The process of spin coating fabrication was optimized for the best fabrication of CuO:Cr thin films, such as the SLG substrate temperature being fixed at 230 ^{O}C. The coated CuO:Cr films were subjected to characterization using advanced techniques. In order to investigate the crystallite parameters, purity, and phase of films, an XRD (Cu-Kα source with wavelength of around 0.154 nm for $\theta - 2\theta$ range in the steps of 0.02^{o}) was used. The surface morphology of the coated Cr:CuO thin films on the soda lime glass (SLG) substrate was studied by scanning electron microscope (a Quanta FEG 250 scanning electron microscope). UV-Vis spectrophotometer (Shimadzu UV-3600, Tokyo, Japan) was used to calculate the absorption data and energy gap in a wavelength range of 300–1100 nm at room temperature. Moreover, 1% and 3% Cr-doped Mo/CuO/*n*-ZnO/i-ZnO/AZO solar cells have been theoretically modelled and the PV parameters of solar cells have been analysed using SCAPD-1D simulation program.

3. Results and Discussion

Figure 1 indicates that XRD patterns of Cr:CuO (1%) and Cr:CuO (3%) thin film demonstrate a characteristic monoclinic CuO structure with a C2/c space group. The diffraction peaks at (-111), (111), (-202), (020), (-311), and (113) are indexed to CuO phase (JCPDS 05-6661). The observed peaks in the high-intensity diffraction spectra suggest that thin films belong to crystallized CuO. Further, the doping ratio changes the XRD pattern of the coated thin film, stating that there is a change of structure in doping in the Cr (1%) and Cr (3%). It can be noticed that the increasing Cr ratio in CuO has made the main peaks more intense.

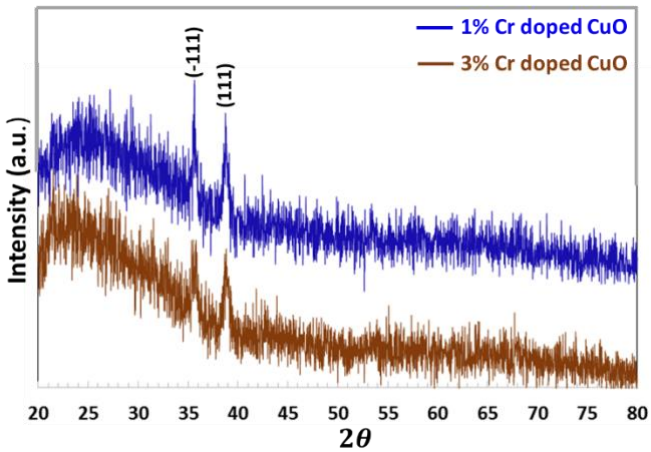

Figure 1. XRD pattern of 1% Cr and 3% Cr-doped CuO thin films.

Our previous study indicates the detailed diffraction information collected from XRD data, including peak orientations (*hkl*), micro- strain (ε), crystallite size (D), dislocation density (δ), and value of inter-planar spacing (d) for (-111) and (111) peaks [18]. The results of the previous study indicate that the crystallite parameters changed due to an increase in Cr ratio. The change in the crystallite parameters by doping metals into CuO has been earlier reported by different research groups [34-36] and matched with our work.

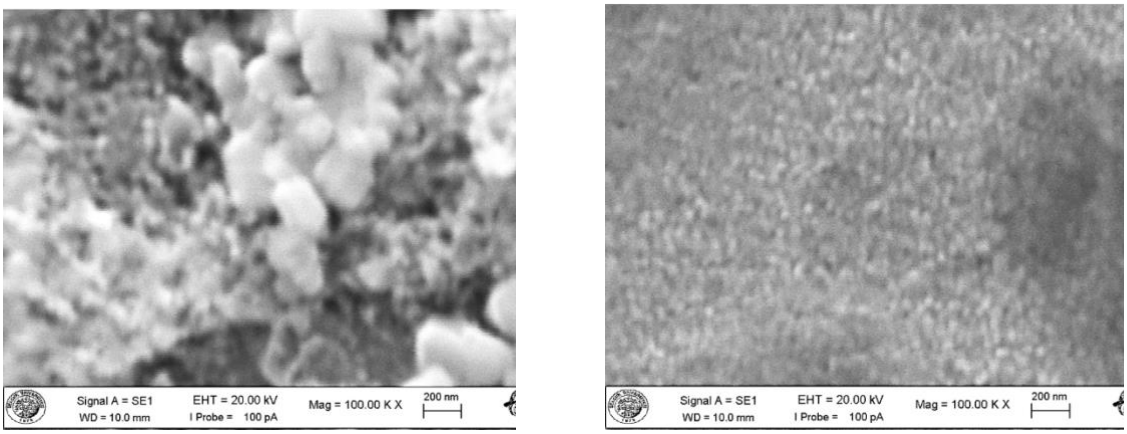

Figure 2. SEM image of **a)** 1% Cr and **b)** 3% Cr-doped CuO thin films.

Figure 2 represents the SEM of Cr:CuO (1%) and Cr:CuO (3%) thin films. The topology of coated film plays an important role in analyzing its optoelectronic properties. An agglomerated morphology can be seen in Figure 2a, whereas a flaky morphology can be realized in Figure 2b. CuO thin films doped with 1% Cr appear slightly different from CuO thin films doped with 3% Cr doping, which is supported by the XRD spectrum. Cr:CuO (1%) and Cr:CuO (3%) thin films exhibit a visible aggregation of particles, showing a little variation in the development of CuO thin films, as shown in the XRD spectrum of thin films. Nanoparticles having the appearance of a flaky ribbon have been widely dispersed over the surface of the substrate, forming a homogenous thin film. These surfaces, which came about as a result of doping CuO thin film, are anticipated to exhibit exceptional optoelectronic capabilities. Dinc et al. indicated that the surface remains homogeneous despite minor clumping caused by Cr-doping. Because of the mild doping, the change in crystallite size is not considerable [37].

3.1. The properties of 1% and 3% Cr-doped CuO thin films

1% Cr-doped CuO thin film absorbs more photons compared to 3% Cr-doped CuO in the visible and UV regions in Figure 3a. The crystallite size of 1% Cr-doped CuO thin film is larger than the crystallite size of 3% Cr-doped CuO thin film, allowing lighter to be absorbed in thin film while limiting its transmission. This shows that 1% Cr-doped CuO thin film is more ideal for use as an absorber layer in PV fields. According to Tauc Plot in the Figures 3b and 3c, the band gaps of 1% Cr and 3% Cr-doped CuO thin films are to be 2.18 eV and 2.30 eV, respectively [18]. Doping with 1% Cr may create shallow defects in the valence band of CuO, which can lead to a decrease in the band gap.

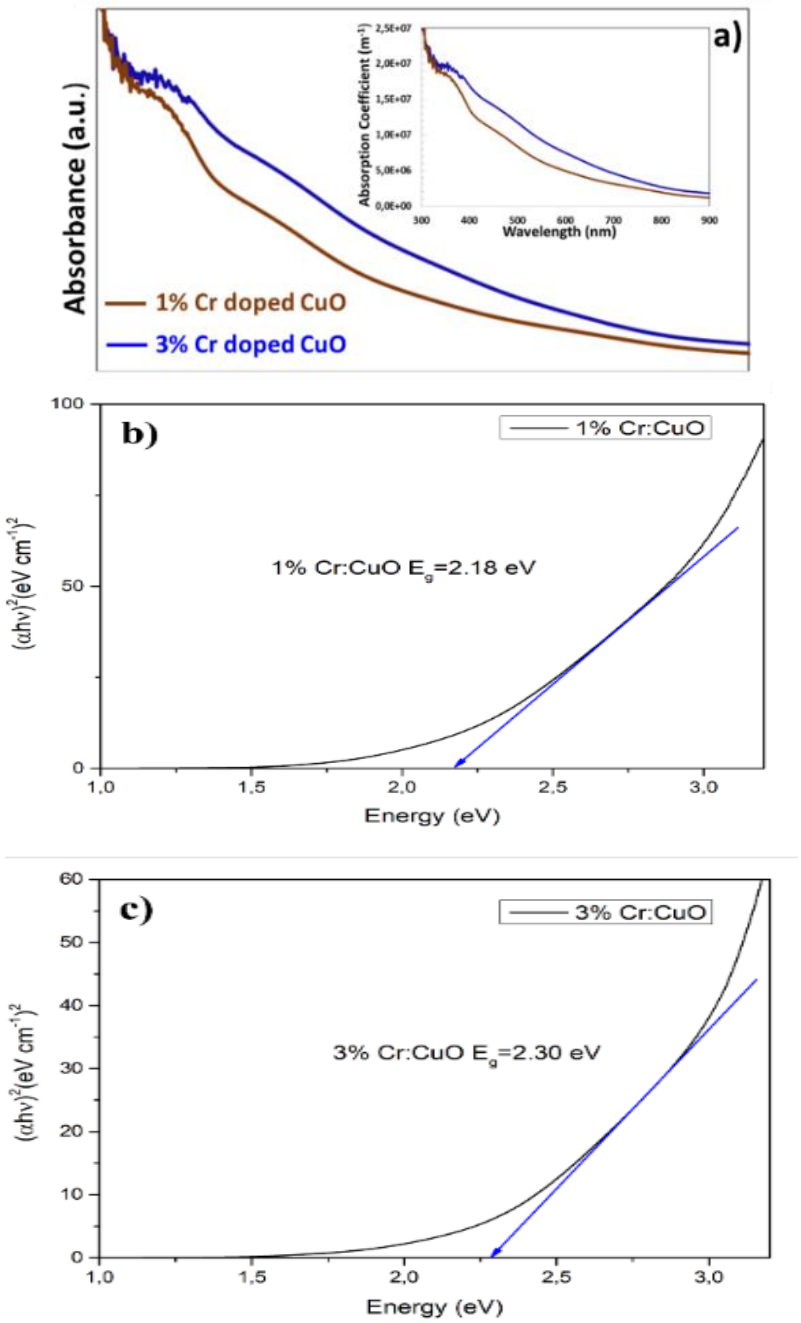

Figure 3. a) The absorbance spectrum **b)** Tauc plot of 1% Cr and **c)** 3% Cr-doped CuO films.

The absorption coefficient (α) of a thin film is expressed by Equation (1) [38]:

$$\alpha = 2.303 * (\frac{A}{W}) \quad (1)$$

A is the absorbance and W is the thin film thickness. 1% Cr-doped CuO thin film indicates a higher absorption coefficient in the Vis and UV regions compared to 3% Cr-doped CuO thin film, as seen in the inset of Figure 3a.

3.2. Modelling of Mo/Cr:CuO/SnO_2/n-ZnO/i-ZnO/AZO thin film solar cells

In this study, SCAPS-1D simulation program [39] was used to model Mo/Cr: CuO/SnO_2/*n*-ZnO/i-ZnO/AZO thin film solar cells as seen Figure 4. In order to model and calculate the electrical parameters of solar cells, the electrical data of all semiconductor layers (given in Table 1) forming the solar cells are input to the program. Experimental data such as band gap, film thickness, absorption coefficient of CuO file (in insert square in Figure 3a) and Cr-doped CuO semiconductors, and values of other layers in literature were used.

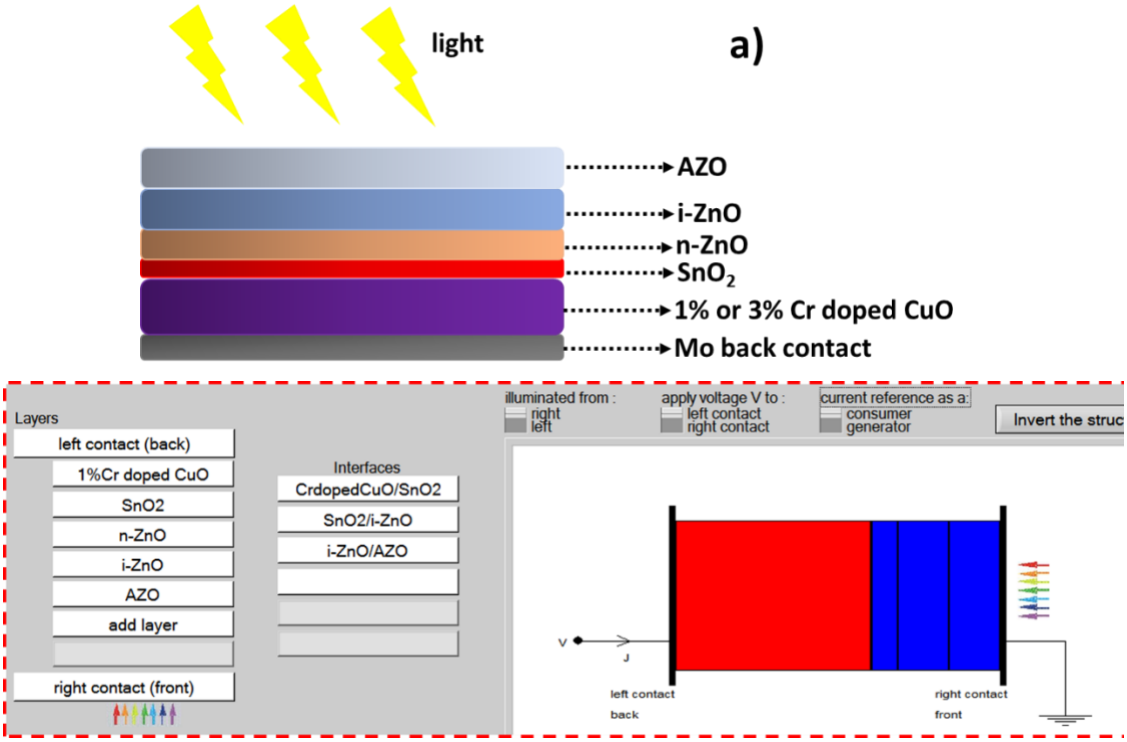

Figure 4. a) The diagram image and **b)** the modelled view of Mo/Cr:CuO/SnO_2/*n*-ZnO/i-ZnO/AZO solar cells.

Table 1. The electrical parameters of semiconductor layers formed Mo/Cr:CuO/SnO_2/*n*-ZnO/i-ZnO/AZO solar cells.

Layers	AZO[40]	i-ZnO [41]	*n*-ZnO	SnO_2	Cr:CuO [42, 43]
Band Gap (eV)	3.3	3.3	3.3	36	2.18/2.30
Electron affinity (eV)	4.6	4.6	4.6	4.5	4.07
Dielectric permittivity (relative)	9	9	9	13.6	11.40/11.43
CB effective density of states (cm^{-3})	$2.20x10^{18}$	$2.20x10^{18}$	$2.20x10^{18}$	$2.20x10^{18}$	$2.20x10^{19}$
VB effective density of states (cm^{-3})	$1.80x10^{19}$	$1.80x10^{19}$	$1.80x10^{19}$	$1.80x10^{19}$	$5.50x10^{20}$
Electron/Hole thermal velocity (cm/s)	$1.00x10^{7}$	$1.00x10^{7}$	$1.00x10^{7}$	$1.00x10^{7}$	$1.00x10^{7}$
Electron/Hole mobility (cm^2/Vs)	100/25	100/25	100/25	100/25	100/20
Shallow donor density (cm^{-3})	$1.00x10^{20}$	$1.00x10^{5}$	0	0	0
Shallow acceptor density (cm^{-3})	0	0	$1.00x10^{18}$	$1.00x10^{16}$	$1.0x10^{16}$
Thickness (nm)	100	100	50	50	380

3.2.1 The effect of the acceptor shallow density (N_a) in Cr:CuO semiconductors on the PV parameters of solar cells

Acceptor defects improve the *p*-type electrical properties of semiconductors. It prevents the recombination of photo-excited charge carriers and increases the number of charge carriers in semiconductors. Thus, a faster and more intense charge transfer takes place in the depletion region. The electrical field increases in the depletion region, and the amount of charge accumulation at the sides increases. Thus, an increase in J_{SC} and V_{OC} value of solar cells occurs [28].

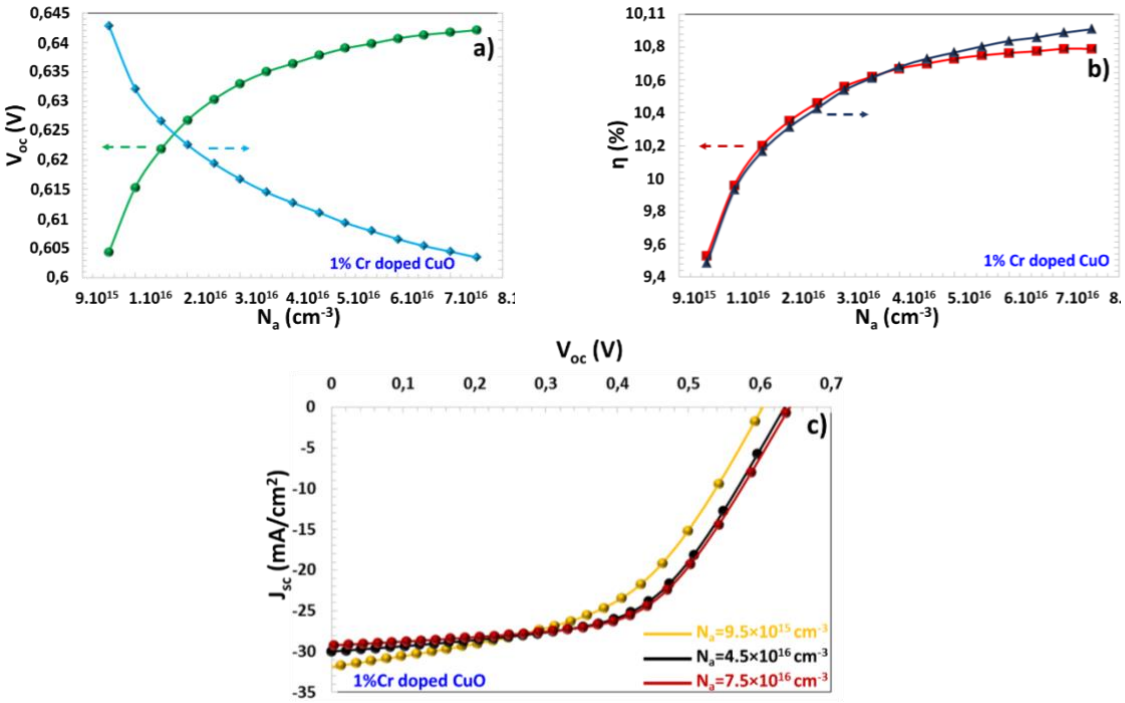

Figure 5. a) ($V_{OC} - J_{SC}$), **b)** (η and FF) vs N_a, and c) $J - V$ for 1% Cr-doped CuO semiconductor.

The N_a dependent ($V_{OC} - J_{SC}$), (η and FF) curves and $J - V$ characteristics of 1% Cr-doped CuO solar cells modelled in this study are given in Figure 5a, 5b and 5c, respectively. As N_a-increased, V_{OC}, η and FF values increased [44], but J_{SC} decreased [45]. Wanda et al indicated that there is a significant potential barrier at the CZTS/Molybdenum interface, as evidenced by the recombination current density at the back-contact, which is estimated to be 3.6 mA/cm^2 [46].This situation can be explained as follows: Some of the photo-excited charge carriers can be trapped by these acceptor defects, and this may cause a decrease in the photocurrent and J_{SC} values. However, since the size of electrical field in the depletion region will cause charge separation, it will increase the charge accumulation at the boundaries of the depletion region and lead to the other PV values to increase [38, 47]. As N_a increases from 9.5×10^{15} cm^{-3} to 7.5×10^{16} cm^{-3}, J_{SC}, V_{OC}, FF and η parameters of 1% Cr:CuO solar cells changed from 31.85 mA/cm^2 to 29.23 mA/cm^2, from 0.604 mV to 0.642 mV, from 49.48% to 57.49%, and from 9.53% to 10.79%, respectively. Adewoyin et al. reported that with an efficiency of 9.39%, the composition ratio of $Cu_2ZnSn_{0.8}Ge_{0.2}S_4$ produced the best $J-V$ characteristics of the top cell, which is lower than our calculated value [40].

The solar cell has shown the highest power conversion efficiency for N_a =7.5×10^{16} cm^{-3}. According to the curves in Figure 6, when the value of N_a increased from 9.5×10^{15} cm^{-3} to 5×10^{16} cm^{-3}, V_{OC}, J_{SC}, FF and η values of 3% Cr:CuO solar cells have been changed from 26.01 mA/cm^2 to 23.92

mA/cm^2, from 0.552 mV to 0.571 mV, from 51.55% to 57.7% and from 7.41% to 7.9%, respectively. Thus, 3% Cr:CuO solar cells exhibits the lower efficiency compared to 1% Cr-doped CuO solar cells. 3% Cr:CuO thin film contains more defects than the other. Also, since 3% Cr-doped CuO thin film absorbs fewer photons, fewer photo-excited charge carriers are formed in the film, resulting in lower efficiency of solar cells.

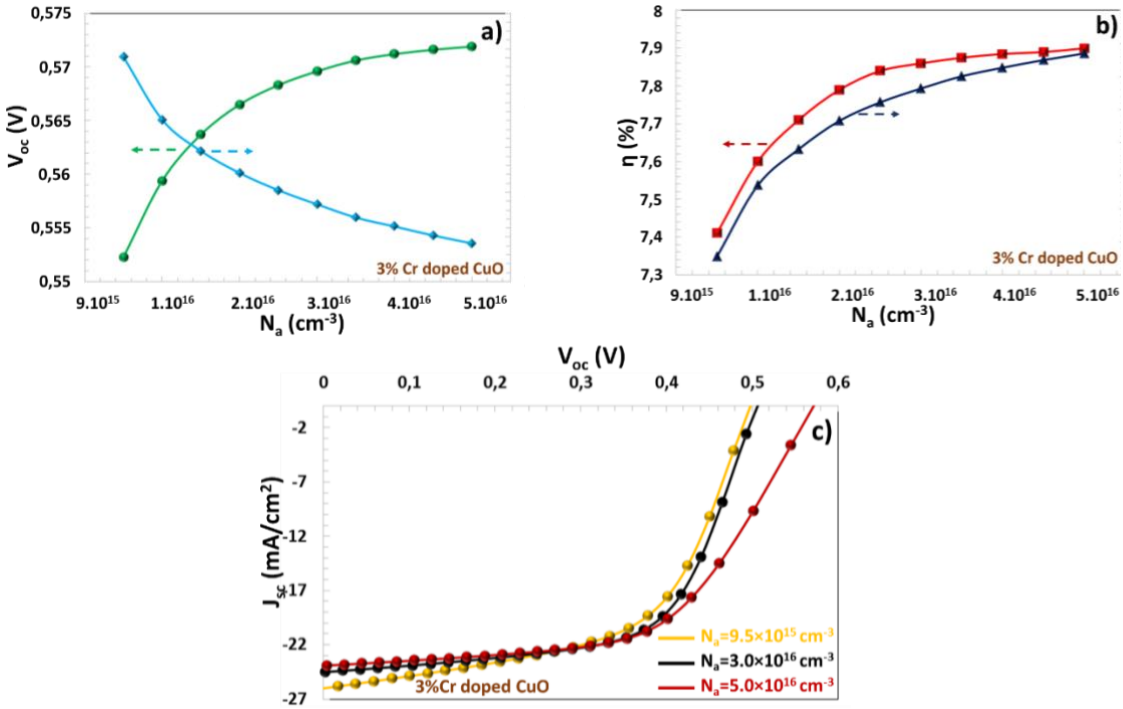

Figure 6. a) ($V_{OC} - J_{SC}$), **b)** (η and FF) vs N_a, and **c)** $J - V$ for 3 % Cr: CuO semiconductor.

3.2.2 The effect of the neutral interface defect density (N_t) in 1% Cr-doped CuO semiconductor on the PV parameters of the solar cells

The defects located between the absorber layer and the buffer layer in the solar cell significantly affect the efficiency of the solar cell. Factors such as lattice mismatch of semiconductors in heterojunction, mismatched band alignment, bond hanging, and doping in the depilation region can cause interface defects [48]. These defects can act as recombination points for electron and hole pairs. The charge transitions are limited by being positioned close to the band edges. Therefore, with increasing defect density, charge accumulation in the depletion region of solar cells decreases, and this causes a decrease in PV parameters [33, 38, 39].

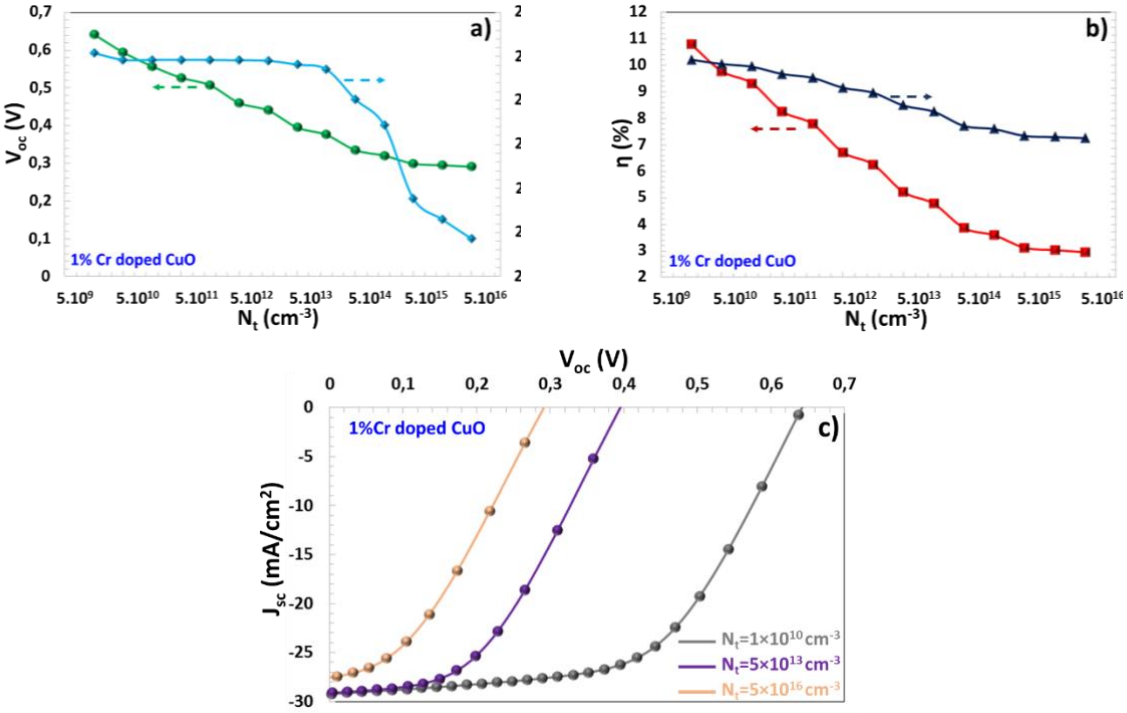

Figure 7. a) ($V_{OC} - J_{SC}$), **b)** (η and FF) vs N_t, and **c)** $J - V$ for 1% Cr:CuO semiconductor.

In this study, since %1 Cr-doped CuO solar cell exhibits higher efficiency, efficiency improvement studies have been carried out on this solar cell. The N_t (neutral defect density) dependent ($V_{OC} - J_{SC}$), (η and FF) curves and $J - V$ characteristics of 1% Cr-doped CuO solar cells have been modelled in the study and are given in Figure 7a, 7b and 7c, respectively. While N_t increases, all electrical parameters of the solar cells decrease. So, N_t rises from 1.0×10^{10} cm^{-3} to 5×10^{16} cm^{-3}, ($V_{OC} - J_{SC}$), (η and FF) values of 1% Cr-doped CuO solar cells have been decreased from 29.23 mA/cm^2 to 27.54 mA/cm^2, from 0.642 mV to 0.291 mV, from 57.49% to 36.75% and from 10.79% to 2.95%, respectively. 1% Cr-doped CuO solar cells has shown the highest power conversion efficiency for N_t =1.0×10^{10} cm^{-3}.

3.2.3 The effect of the SnO_2 layer on the PV performance of 1% Cr:CuO solar cells

According to the band diagram of 1%Cr-doped CuO solar cells in Figure 8a, a cliff-like band [42] was formed between the 1% Cr-doped CuO and the *n*-ZnO heterojunction. A cliff-like conduction band offset leads to trap state-assisted recombination. This causes the charge carriers to decrease and J_{SC} value to deteriorate. In this study, to overcome this problem, a SnO_2 ultrathin intermediate layer in the 3.6 eV band gap [42] that was placed between as shown in the band diagram in Figure 8b. The SnO_2 layer partially forms a spike like conduction band offset, optimizing conduction band alignment. It prevents recombination caused by trap states at the interface [26, 49]. Therefore, SnO_2 blocks the hole charges away from the ZnO buffer layer, which acts as an electron selector for the 1% Cr:CuO active layer as seen in Figure 8c, in order to passivate the interface states.

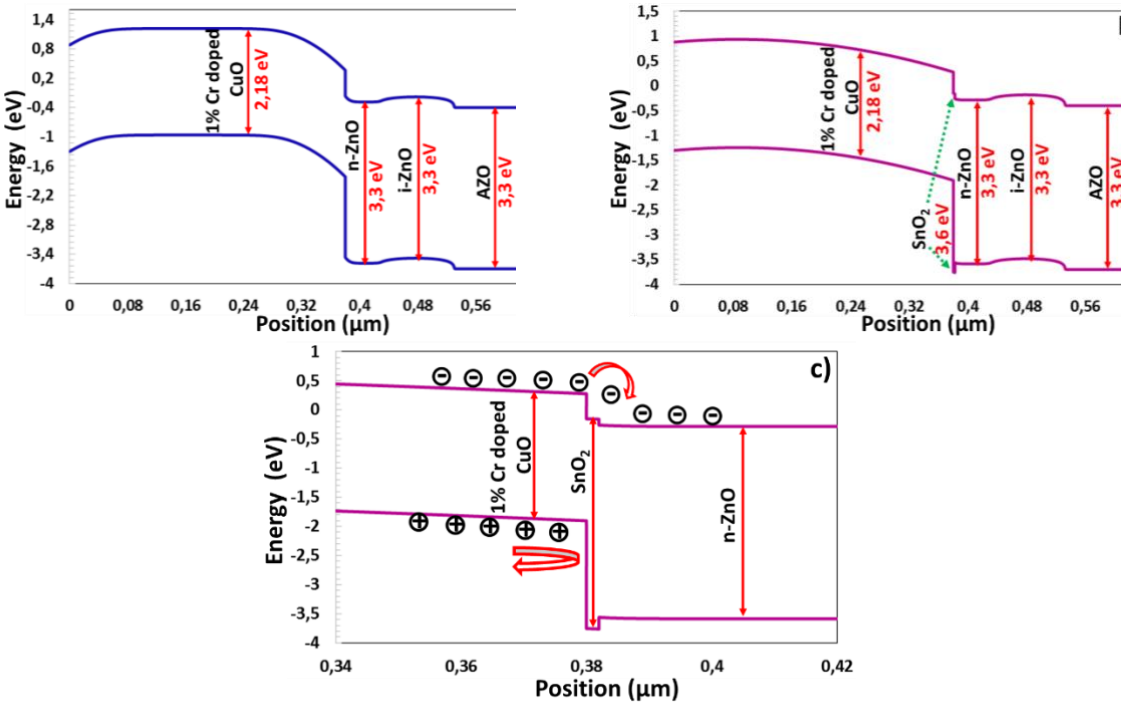

Figure 8. a) The band diagrams of 1% Cr: CuO/*n*-ZnO, **b)** 1% Cr: CuO/SnO_2/*n*-ZnO solar cells and **c)** the charge transfer in 1% Cr:CuO solar cells with SnO_2 intermediate layer.

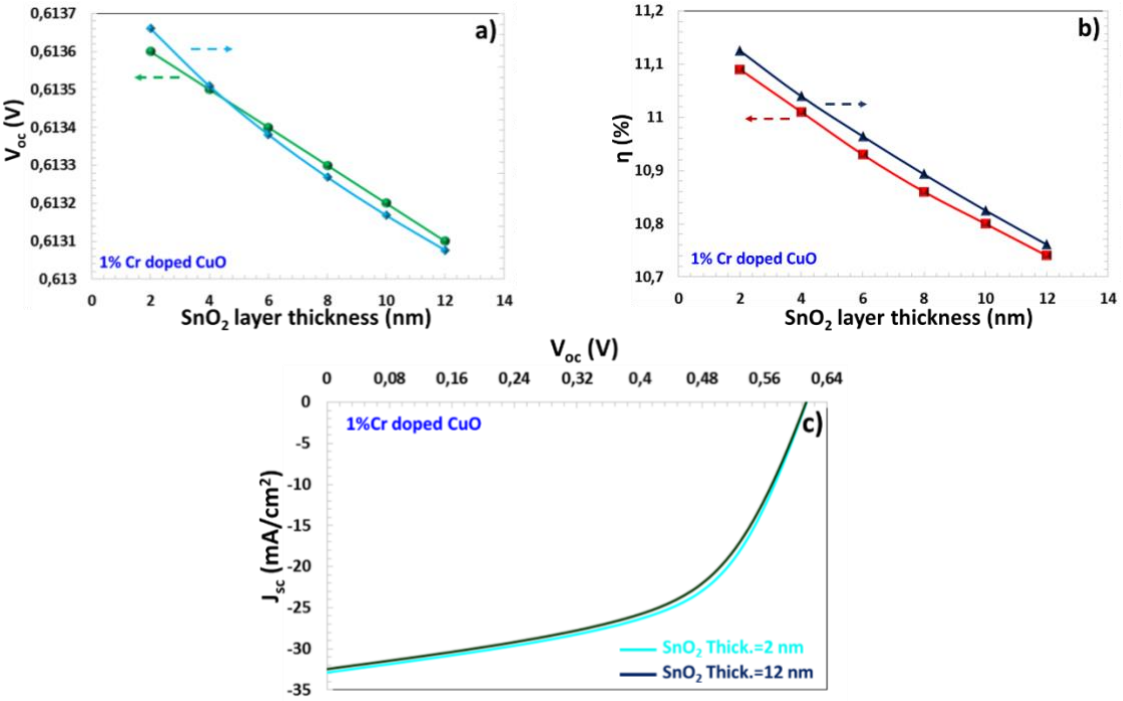

Figure 9. a) ($V_{OC} - J_{SC}$), **b)** (η and FF) vs SnO_2 layer thickness graphs and **c)** $J-V$ characteristics dependent SnO_2 layer thickness for 1% Cr-doped CuO semiconductor.

Figure 9 show that ($V_{OC} - J_{SC}$), (η and FF) vs SnO_2 layer thickness graphs and $J-V$ characteristics-dependent SnO_2 layer thickness (for 2 nm and 12 nm) for 1% Cr:CuO semiconductor. For the solar cells with SnO_2 layer thickness of 2 nm, (J_{SC} =32.9 mA/cm^2, V_{OC} =0.615 mV, FF =54.99% and η = 11.09% while J_{SC} =29.23mA/cm^2, V_{OC} =0.642 mV, FF =57.49% and

η =10.79% to solar cells without SnO_2 layer. Sun et al. indicate that CZTS solar cells with SnO_2 intermediate layers have an improved overall efficiency of 6.82% to 8.47% due to their higher V_{OC} of 657 mV and FF of 62.8% when compared to their counterpart cells without the SnO_2 intermediate layer, which have V_{OC} of 638 mV and FF of 52.4% [30]. As stated above, SnO_2 layer provided the ideal charge transition in the band structure. Thus, the photo-excited charge carriers in the depletion region contribute to charge aggregation at the edges and do not adversely affect the shunt resistance, resulting in higher J_{SC} and efficiency values. However, although SnO_2 layer thickness of 2 nm is low, it can cause a large electrical field in the depletion region and trap states for charge carriers in the band gap. This causes V_{OC} and FF values to be slightly lower. However, the high J_{SC} value resulted in higher efficiency compared to η value of solar cells without SnO_2 layer. As SnO_2 film thickness increases from 2 nm to 12 nm, J_{SC}, V_{OC}, FF and η values of 1% Cr-doped CuO solar cells with SnO_2 layer decreases from 32.87 mA/cm^2 to 32.45 mA/cm^2, from 0.613,6 mV to 0.613,1 mV, from 54.99% to 53.97% and from 11.09% to 10.74%, respectively. The higher thickness of SnO_2 layer reduces the electrical field in the depletion region and may limit charge separation. Thus, in interfacial trap states, charge carriers may undergo recombination resulting in degradation of PV performance.

4. Conclusions

In this study, 1% and 3% Cr-doped CuO thin film has been produced by spin coating system. XRD spectra indicates that all of thin films coated had a polycrystalline nature, with preferential (-111) and (111) orientations. Cr doping ratio changes XRD pattern of thin film coated and increments in Cr ratio in CuO have made the main peaks more intense. SEM images reveals that the agglomerated morphology can be seen in CuO:Cr (1%), whereas flaky morphology can be seen in CuO:Cr (3%). 1% Cr-doped CuO thin film absorbs more photons compared to 3% Cr-doped CuO in Vis and UV regions. The band gaps of 1% Cr and 3% Cr-doped CuO thin films have been determined to be 2.18 eV and 2.30 eV, respectively. Using the SCAPS simulation program, the solar cells consisting of Mo/1% and 3% Cr-doped Mo/Cr:CuO/SnO_2/*n*-ZnO/i-ZnO/AZO layers have been modelled. With some increases in N_t neutral defect density, all PV parameters of these solar cells deteriorated. However, 1% Cr-doped CuO solar cells performed better than 3% Cr:CuO solar cells. With the increase of N_a acceptor defect density, while J_{SC} value decreased, V_{OC}, FF and η values of 1% Cr-doped CuO solar cells increased. At the interface, SnO_2 intermediate thin layer with thickness between 2 nm and 12 nm that was put on the interface to passivate the defect, trap structures, and to provide ideal charge transfer (hole and electron). The solar cells with SnO_2 intermediate layer at 2 nm thickness showed higher J_{SC} , FF and η values compared to solar cells without any intermediate layer.

Ethical statement:

The authors declare that this study does not require ethics committee approval or any special permission.

Acknowledgements:

Authors would kindly like to thank to

- Selcuk University, Scientific Research Projects (BAP) Coordination Office for the support with the number 15201070 and 19401140 projects,
- Selçuk University, High Technology Research and Application Center (İL-TEK) and
- SULTAN Center for infrastructures
- Dicle University Scientific Research Project (BAP) Coordination office
- Dr. Marc Burgelman's group, University of Gent, Belgium for providing permission for us to use SCAPS-1D simulation program.

Conflict of interest:

The authors declare no conflicts of interest.

Authors' Contributions:

S. Y. G: Conceptualization, Formal analysis, Writing first draft preparation (30%)
S. B: Conceptualization, Methodology, Resources (%25).
I.C: Formal analysis, draft preparation (%20)
H. S. K: Formal analysis, draft preparation, project coordinator (%25)
All authors read and approved the final manuscript.

References

[1] Sultana, J., Das, A., Saha, N. R., Karmakar, A., and Chattopadhyay, S., "Characterization of nano-powder grown ultra-thin film p-CuO/n-Si hetero-junctions by employing vapour-liquid-solid method for photovoltaic applications," *Thin Solid Films*, 612, 331-336, 2016.

[2] Sultana, J., Paul, S., Karmakar, A., Yi, R., Dalapati, G. K., and Chattopadhyay, S., "Chemical bath deposited (CBD) CuO thin films on n-silicon substrate for electronic and optical applications: Impact of growth time," *Applied surface science*, 418, 380-387, 2017.

[3] Salari, H., and Sadeghinia, M., "MOF-templated synthesis of nano Ag2O/ZnO/CuO heterostructure for photocatalysis," *Journal of Photochemistry and Photobiology A: Chemistry*, 376, 279-287, 2019.

[4] Sharma, D., Prajapati, A. K., Choudhary, R., Kaushal, R. K., Pal, D., and Sawarkar, A. N., "Preparation and characterization of CuO catalyst for the thermolysis treatment of distillery wastewater," *Environmental technology*, 39(20), 2604-2612, 2018.

[5] Zhang, Y., *et al.*, "CuO@ Ag core-shell material preparation and as high-stability anodes for lithium-ion batteries," *Powder Technology*, 355, 386-392, 2019.

[6] Eibl, O., "Application of a new method for absorption correction in high-accuracy, quantitative EDX microanalysis in the TEM: analysis of oxygen in CuO-based high-Tc superconductors," *Ultramicroscopy*, 50(2), 189-201, 1993.

[7] Lokhande, P. E., and Chavan, U. S., "Surfactant-assisted cabbage rose-like CuO deposition on Cu foam by for supercapacitor applications," *Inorganic and Nano-Metal Chemistry*, 48(9), 434-440, 2018.

[8] Ates, M., Garip, A., Yörük, O., Bayrak, Y., Kuzgun, O., and Yildirim, M., "rGO/CuO/PEDOT nanocomposite formation, its characterisation and electrochemical performances for supercapacitors," *Plastics, Rubber and Composites*, 48(4), 168-184, 2019.

[9] Park, K.-R., Cho, H.-B., Lee, J., Song, Y., Kim, W.-B., and Choa, Y.-H., "Design of highly porous SnO2-CuO nanotubes for enhancing H2S gas sensor performance," *Sensors and Actuators B: Chemical*, 302, 127179, 2020.

[10] Shaban, M., Abdelkarem, K., and El Sayed, A. M., "Structural, optical and gas sensing properties of Cu2O/CuO mixed phase: effect of the number of coated layers and (Cr+ S) co-Doping," *Phase Transitions*, 92(4), 347-359, 2019.

[11] Budhiraja, N., Kumar, V., Tomar, M., Gupta, V., and Singh, S., "Facile synthesis of porous CuO nanosheets as high-performance NO2 gas sensor," *Integrated Ferroelectrics*, 193(1), pp. 59-65, 2018.

[12] Sheikholeslami, M., "Solidification of NEPCM under the effect of magnetic field in a porous thermal energy storage enclosure using CuO nanoparticles," *Journal of Molecular Liquids*, 263, 303-315, 2018.

[13] Tan, R., *et al.*, "Enhanced open-circuit photovoltage and charge collection realized in pearl-like NiO/CuO composite nanowires based p-type dye sensitized solar cellss," *Materials Research Bulletin*, 116, 131-136, 2019.

[14] Ayed, R. B., Ajili, M., Thamri, A., Kamoun, N. T., and Abdelghani, A., "Substrate temperature effect on the crystal growth and optoelectronic properties of sprayed α-Fe2O3 thin films: application to gas sensor and novel photovoltaic solar cells structure," *Materials Technology*, 33(12), 769-783, 2018.

[15] Mageshwari, K., Sathyamoorthy, R., and Park, J., "Photocatalytic activity of hierarchical CuO microspheres synthesized by facile reflux condensation method," *Powder Technology*, 278, 150-156, 2015.

[16] Elango, M., Deepa, M., Subramanian, R., and Mohamed Musthafa, A., "Synthesis, characterization, and antibacterial activity of polyindole/Ag–Cuo nanocomposites by reflux condensation method," *Polymer-Plastics Technology and Engineering*, 57(14), 1440-1451, 2018.

[17] Joseph, A., *et al.*, "An experimental investigation on pool boiling heat transfer enhancement using sol-gel derived nano-CuO porous coating," *Experimental Thermal and Fluid Science*, 103, 37-50, 2019.

[18] Baturay, S., Candan, I., and Ozaydın, C., "Structural, optical, and electrical characterizations of Cr-doped CuO thin films," *Journal of Materials Science: Materials in Electronics*, 33(9), 7275-7287, 2022.

[19] Liu, X., Xu, W., Xu, M., Hao, X., and Feng, X., "Epitaxial CuO thin films prepared on MgAl2O4 (110) by RF-plasma assisted pulsed laser deposition," *Vacuum*, 169, 108932, 2019.

[20] Tang, C., Sun, F., Chen, Z., Chen, D., and Liu, Z., "Improved thermal oxidation growth of non-flaking CuO nanorod arrays on Si substrate from Cu film and their nanoscale electrical properties for electronic devices," *Ceramics International*, 45(12), 14562-14567, 2019.

[21] Mahmood, A., Tezcan, F., and Kardaş, G., "Photoelectrochemical characteristics of CuO films with different electrodeposition time," *International journal of hydrogen energy*, 42(36), 23268-23275, 2017.

[22] Sahu, A. K., Das, A., Ghosh, A., and Raj, S., "Understanding blue shift of the longitudinal surface plasmon resonance during growth of gold nanorods," *Nano Express*, 2(1), 010009, 2021.

[23] Aslam, M., Raza, Z. A., and Siddique, A., "Fabrication and chemo-physical characterization of CuO/chitosan nanocomposite-mediated tricomponent PVA films," *Polymer Bulletin*, 78, 1955-1965, 2021.

[24] Aslam, M., Kalyar, M. A., and Raza, Z. A., "Fabrication of nano-CuO-loaded PVA composite films with enhanced optomechanical properties," *Polymer Bulletin*, 78, 1551-1571, 2021.

[25] Shinde, S., *et al.*, "Effect of deposition parameters on spray pyrolysis synthesized CuO nanoparticle thin films for higher supercapacitor performance," *Journal of Electroanalytical Chemistry*, 850, 113433, 2019.

[26] Sun, H., *et al.*, "Efficiency enhancement of kesterite Cu_2ZnSnS_4 solar cellss via solution-processed ultrathin tin oxide intermediate layer at absorber/buffer interface," *ACS Applied Energy Materials*, 1(1), 154-160, 2017.

[27] Pearton, S., Norton, D., Ip, K., Heo, Y. and Steiner, T., "Recent advances in processing of ZnO", *Journal of Vacuum Science&Technology B: Microelectronics and Nanometer Structures Processing, Measurement, and Phenomena*, 22, 932–48, 2004

[28] Look, D.C., "Recent advances in ZnO materials and devices", *Materials Science and Engineering: B* 80, 383–7, 2001

[29] Van de Walle, C.G ., "Hydrogen as a cause of doping in zinc oxide", *Physical Review Letters*, 85, 1012, 2000

[30] Look, D.C., Hemsky, J.W, and Sizelove, J., "Residual native shallow donor in ZnO", *Physical Review Letters*, 82, 2552, 1999

[31] Piñón Reyes, A. C., *et al.*, "Study of a lead-free perovskite solar cell using CZTS as HTL to achieve a 20% PCE by SCAPS-1D simulation," *Micromachines*, 12(12), 1508, 2021.

[32] AlZoubi, T., Moghrabi, A., Moustafa, M., and Yasin, S., "Efficiency boost of CZTS solar cellss based on double-absorber architecture: Device modeling and analysis," *Solar Energy*, 225, 44-52, 2021.

[33] Houimi, A., Gezgin, S. Y., Mercimek, B., and Kılıç, H. Ş., "Numerical analysis of CZTS/n-Si solar cellss using SCAPS-1D. A comparative study between experimental and calculated outputs," *Optical Materials*, 121, 111544, 2021.

[34] Gnanasekar, T., *et al.*, "Enhanced opto-electronic properties of X-doped (X= Al, Ga, and In) CuO thin films for photodetector applications," *Journal of Materials Science: Materials in Electronics*, 33(23), 18786-18797, 2022.

[35] Naveena, D., Logu, T., Dhanabal, R., Sethuraman, K., and Bose, A. C., "Comparative study of effective photoabsorber CuO thin films prepared via different precursors using chemical spray pyrolysis for solar cells application," *Journal of Materials Science: Materials in Electronics*, 30, 561-572, 2019.

[36] Devi, L. V., Selvalakshmi, T., Sellaiyan, S., Uedono, A., Sivaji, K., and Sankar, S., "Effect of La doping on the lattice defects and photoluminescence properties of CuO," *Journal of Alloys and Compounds*, 709, 496-504, 2017.

[37] Dinc, S., Şahin, B., and Kaya, T., "Improved sensing response of nanostructured CuO thin films towards sweat rate monitoring: effect of Cr doping". *Materials Science in Semiconductor Processing*, 105, 104698, 2020

[38] Gezgin, S. Y., "Modelling and investigation of the electrical properties of CIGS/n-Si heterojunction solar cellss," *Optical Materials*, 131, 112738, 2022.

[39] Yiğit Gezgin, S., and Kiliç, H. Ş., "The effect of Ag plasmonic nanoparticles on the efficiency of CZTS solar cells: an experimental investigation and numerical modelling," *Indian Journal of Physics*, **97**(3), 779-796, 2023.

[40] Adewoyin, A. D., Olopade, M. A., Oyebola, O. O., and Chendo, M. A., "Development of CZTGS/CZTS tandem thin film solar cells using SCAPS-1D," *Optik*, 176, 132-142, 2019.

[41] AlZoubi, T., and Moustafa, M., "Numerical optimization of absorber and CdS buffer layers in CIGS solar cellss using SCAPS," *Int. J. Smart Grid Clean Energy*, 8, 291-298, 2019.

[42] Lam, N. D., "Modelling and numerical analysis of ZnO/CuO/Cu_2O heterojunction solar cells using SCAPS," *Engineering Research Express*, 2(2), p. 025033, 2020.

[43] Gezgin, S. Y., Candan, I., Baturay, S., Kilic, H. S., "Structural, Morphological, Optical Properties and Modelling of Ag Doped CuO/ZnO/AZO Solar Cells," *Journal of Coating Science and Technology*, 9, 26-37, 2022/11/21.

[44] Djinkwi Wanda, M., Ouédraogo, S., Tchoffo, F., Zougmoré, F., and Ndjaka, J., "Numerical investigations and analysis of Cu_2ZnSnS_4 based solar cellss by SCAPS-1D," *International Journal of Photoenergy*, 2016, 2016.

[45] Gupta, G. K., and Dixit, A., "Simulation studies of CZT (S, Se) single and tandem junction solar cellss towards possibilities for higher efficiencies up to 22%," *arXiv preprint arXiv:1801.08498*, 2018.

[46] Gezgin, S. Y., Candan, İ., Baturay, Ş., and Kiliç, H. Ş., "Modelling Of The Solar Cell Based On Cu_2SnS_3 Thin Film Produced By Spray Pyrolysis," *Middle East Journal of Science*, 8(1), 64-76, 2022.

[47] Kaur, K., Kumar, N., and Kumar, M., "Strategic review of interface carrier recombination in earth abundant Cu–Zn–Sn–S–Se solar cells: current challenges and future prospects," *Journal of Materials Chemistry A*, 5(7), 3069-3090, 2017.

[48] Mounkachi, O., *et al.*, "Band-gap engineering of SnO_2," *Solar Energy Materials and Solar Cellss*, 148, 34-38, 2016.

[49] Guirdjebaye, N., Ngoupo, A. T., Ouédraogo, S., Tcheum, G. M., and Ndjaka, J., "Numerical analysis of CdS-CIGS interface configuration on the performances of Cu(In,Ga)Se_2 solar cells," *Chinese Journal of Physics*, 67, 230-237, 2020.

Middle East Journal of Science

https://dergipark.org.tr/mejs **MEJS**

e-ISSN:2618-6136

Research Article

A LAGRANGE NEURAL NETWORK FOR NETWORK TRAFFIC ASSIGNMENT OPTIMIZATION

Hasan Dalman*[1]

[1]Batman University, Department of Mathematics, Batman, Türkiye
Corresponding author; hasan.dalman@batman.edu.tr

Abstract: *A solution to the challenge of assigning static network traffic is being sought through this research. To address this issue, a model that uses the Lagrange function has been developed. The Lagrange neural network is a dynamic system that is created by calculating the function's gradient in relation to its variables. This system comprises differential equations that are adapted based on the initial conditions. The theoretical properties of this network are delved into in the paper, including its overall and local stability, and it is proven that the system exhibits global stability. Equilibrium points achieved by numerically solving the network meet the Karush-Kuhn-Tucker requirements, as demonstrated by using the Lyapunov method. It is guaranteed that they will converge towards the user equilibrium of the original problem. Finally, the effectiveness of the presented approach is showcased by providing a numerical example. The results obtained using this approach outperform those obtained using the Frank-Wolfe method.*

Keywords*: Dynamical systems, Graph theory, Lagrange neural network, Network traffic assignment*

Received: March 28, 2023 *Accepted: October 18, 2023*

1. Introduction

In the field of transportation engineering and urban planning, traffic assignment models are essential tools. These models offer valuable insights into how vehicular traffic moves through a network of roads and infrastructure. By helping planners and decision-makers optimize traffic management, reduce congestion, and upgrade transportation systems, they play a crucial role in improving overall transportation efficiency.

However, traffic assignment has been a challenging problem for transportation engineers for quite some time. Initially, mathematical models were created to understand how traffic moves through cities, assuming that drivers always choose the shortest route. However, this assumption was found to be inaccurate. Drivers may select longer routes if they believe it will save time or help them avoid certain roads or areas. As a result, more sophisticated traffic assignment models have been developed that consider driver preferences. These models can predict traffic flow, enabling planners to make informed decisions to optimize traffic flow.

Wardrop's research [1] has fundamentally established that in the realm of transportation, travelers do not possess the ability to reduce their travel time merely by opting for an alternative route. This fundamental principle, commonly referred to as User Equilibrium (UE), has emerged as a cornerstone in the domain of traffic assignment. Subsequently, this concept has undergone extensive development and refinement by numerous scholars, rendering it the prevailing standard for the evaluation of traffic assignment algorithms in contemporary practice. Addressing this intricate challenge necessitates a

diverse array of models and algorithms, spanning from rudimentary heuristics to sophisticated optimization techniques.

One advanced approach in the field of transportation engineering is the Frank-Wolfe algorithm, which was originally introduced to address the challenging problem of traffic assignment [2]. Beckmann and his colleagues [5] made significant strides in this domain by transforming the UE condition into a nonlinear convex programming problem. This transformation paved the way for the development of efficient algorithms tailored to tackle the UE condition. In a similar vein, Daganzo and Sheffi [4] pioneered a distinctive traffic assignment methodology grounded in the concept of traffic equilibrium, while Sheffi and Powell [3] provided a comprehensive analysis of this issue along with potential remedies. In addition to these fundamental contributions, various alternative methodologies have emerged for predicting User Equilibrium. These include sequential averages ([3], [5]), simulated annealing ([6]), and the application of game theory ([25]). Notably, Javani and Babazadeh [26] introduced an algorithm that identifies descent directions through iterative solutions of a series of quadratic programming subproblems within the framework of truncated quadratic programming. This method, formally known as OD-based Frank-Wolfe truncated quadratic programming, systematically addresses each quadratic programming subproblem associated with Origin-Destination (OD) pairs. These subproblems are efficiently solved using the Frank-Wolfe optimization technique, taking into account only the active paths. The authors introduced a path-based algorithm designed for static traffic assignment problems. This algorithm leverages the Wolfe reduced gradient method, column generation, and speed-up techniques to optimize traffic flow allocation efficiently. It demonstrates superior convergence performance when compared to reference algorithms, as evidenced by testing on scenarios presented in [27].

For an exhaustive compilation of optimization models related to the traffic assignment problem, along with a thorough exposition of the solution methodologies applied to these models, readers are encouraged to consult [22] and [23]. Additionally, for a current overview of research on UE, we recommend referring to [28].

In the context of solving traffic assignment optimization problems subject to specific constraints, the Lagrange function emerges as an invaluable tool for achieving optimality. This specialized function amalgamates the objective function with constraints to maximize the solution while satisfying both the objective and the constraints, constituting what is known as the Lagrange dual problem [22]. By leveraging the gradient of the Lagrange function, a system of differential equations can be derived. Given that the primary purpose of the Lagrange function in network traffic assignment problems is to minimize system variables, the derivatives of these variables with respect to time must exhibit a decreasing trend in the negative direction. Simultaneously, in pursuit of maximizing the Lagrange variables embedded within the Lagrange function, their derivatives must manifest an ascending trajectory in the positive direction. This intricate interplay yields a system of equations that bears a resemblance to an artificial neural network, thus being denoted as a Lagrange programming neural network [17]. This neural network variant finds application in diverse mathematical optimization contexts.

To construct a Lagrange programming neural network (LPNN), a conventional neural network architecture is augmented with a specialized layer responsible for computing the Lagrange multipliers associated with constraints. The mathematical underpinnings of LPNN and its training process through the backpropagation algorithm are expounded upon in this paper. Furthermore, a mathematical rendition of the Lagrange neural network grounded in the duality theorem is presented in [18-20], where the authors furnish empirical evidence substantiating the efficacy of these methodologies in addressing a spectrum of optimization challenges ([19], [20]). In [24], the authors introduce an artificial neural

network method tailored for traffic assignment, particularly aimed at optimizing the duration of green signals at traffic intersections, culminating in observed enhancements in traffic flow.

To the best of our knowledge, the utilization of Lagrange neural networks to optimize network traffic assignment problems has not been explored in existing literature. Thus this study centers on addressing a network traffic assignment problem through the application of a neural network approach. Furthermore, it transitions the initially static network traffic assignment problem into a dynamic one, allowing an examination of how traffic flows on connections evolve over time. To establish this dynamic framework, a differential equation system is formulated using the Lagrange function, interpreting the given network traffic assignment problem as a neural network. The stability of this system and its convergence towards user equilibrium are demonstrated with the aid of a Lyapunov function. Lastly, a numerical example is presented to elucidate the solution process.

Here is the structure of the paper: The second section presents the optimization problem concerning network traffic assignment UE, and the Karush-Kuhn-Tucker criteria. Section 3 introduces the Lagrange function and outlines the creation of a Lagrange neural network. A numerical example is given in Section 4, and concluding remarks are provided in Section 5. This text contains instructions for preparing manuscripts for the journal.

2. Mathematical Formulation

2.1. Constrained Nonlinear Optimization for The Network Traffic Assignment Problem

The theory of UE is of utmost importance in transportation engineering. It provides valuable insights into traffic behavior within a network. According to this theory, drivers opt for the most efficient route to reach their destination based on travel time. As more drivers make informed decisions, the network reaches a state of equilibrium where no one can improve their travel time by switching routes. This equilibrium flow is a reliable mechanism for approximating traffic patterns in any given network.

The primary aim is to achieve a balanced distribution of traffic across all edges, denoted as $e \in E$, in a connected directed graph $G = (V, E)$. This distribution is dictated by the traffic demand F^w for each origin-destination (OD) pair $w \in W$, with the ultimate objective of attaining UE. Under UE conditions, travel times on all utilized routes are equal and do not surpass those of any unused routes.

This model defines the symbol G as a network that comprises a collection of vertices denoted as V and a group of edges identified as E that connect these vertices. The set W includes all origin-destination pairs that exist within the network. Each pair of origin-destination, denoted as $w \in W$ the set R^w comprises all possible routes that connect the origin and destination of that specific pair. The flow of traffic through each edge $e \in E$ is depicted by the vector $x = (\ldots, x_e, \ldots)$ x_e^w, representing the traffic flow through the edge e for the OD pair w. The capacity of each edge $e \in E$ is illustrated by the vector $c = (\ldots, c_e, \ldots)$, whi $t_e(x_e)$ ch is a function that confidently models the travel time (delay) of the flow x_e through a congested edge e.

The problem of traffic assignment is tackled by formulating it as a nonlinear optimization problem that aims to achieve UE ([21]). The problem can be mathematically described as follows:

$$\begin{aligned} &\min_{x(f)} \sum_{e\in E} \int_0^{x_e(f)} t_e(u)du \\ &\text{subject to} \\ &F^w - \sum_{r\in R^w} f_r^w = 0, \quad \forall w \in W \\ &f_r^w \geq 0, \forall r \in R^w, w \in W \end{aligned} \tag{1}$$

The problem is accompanied by predefined constraints, where $x_e\left(f_r^w\right) = \sum_{w\in W}\sum_{r\in R^w} f_r^w \delta_{e,r}^w \quad \forall e \in E$.

The relevant variables are:

* f represents the traffic flow on all edges
* $x_e(f)$ denotes the flow-dependent travel time on the edge e
* $t_e(u)$ represents the travel time function on the edge e
* F^w stands for the demand for OD pair w
* R^w is the set of routes for the OD pair w
* f_r^w denotes the flow on route r for the OD pair w
* $\delta_{e,r}^w$ is the Kronecker delta, which is 1 if the edge e is on the route r and 0 otherwise.

The main objective of the problem (1) is to minimize the total travel time (or total travel cost) for all traffic flows. This can be achieved by implementing the first set of constraints, which ensures that the demand for each OD pair is met by the traffic flows on the network. Additionally, the second set of constraints guarantees that the traffic flow on each route is always non-negative. Lastly, the definitional constraints establish a link between the traffic flow on each edge and the traffic flow on each route.

2.2. Karush Kuhn Tucker (KKT) Conditions For The Nonlinear Network Traffic Assignment Problem

It is crucial to abide by the constraints of problem (1) when dealing with traffic assignment problems. To achieve optimization, it is imperative to satisfy the Karush-Kuhn-Tucker (KKT) conditions. These conditions provide a framework for the requirements to attain a feasible solution. If all KKT conditions are met and the optimization problem is convex, then the solution is guaranteed to be optimal. To obtain the Lagrange function for the traffic assignment problem (1), Lagrange multipliers must be added for each constraint of the problem (1) and included in the objective function.

Thus the Lagrangian function, which solves the problem, is expressed below:

$$\mathrm{L}(x(f),\lambda) = \sum_{e\in E} \int_0^{x_e(f)} t_e(u)du + \sum_{w\in W} \lambda_r^w \left(F^w - \sum_{r\in R^w} f_r^w \right) \tag{2}$$

It consists of flow variables $x_e(f)$ and Lagrange multipliers λ_r^w.

The first term in function (2) represents the total travel time on all edges concerning the flow variable f, which is the same as the objective function of problem (1).

The second term includes the Lagrange multiplier associated with demand constraints, ensuring that the total traffic demand between each OD pair is satisfied.

The third term includes the Lagrange multiplier associated with flow constraints, ensuring that the flow on each route is non-negative. The Lagrange multiplier λ_r^w represents both the flow conservation constraint and the non-negativity constraint.

In order to optimize problem (1), we can re-write the function (2) by substituting all $e \in E$ with $x_e = \sum_{w \in W} \sum_{r \in R^w} f_r^w \delta_{e,r}^w$. This leads to the following result:

$$\mathrm{L}(f, \lambda) = \sum_{e \in E} \int_0^{\sum_{w \in W} \sum_{r \in R^w} f_r^w \delta_{e,r}^w} t_e(u) du + \sum_{w \in W} \lambda_r^w \left(F^w - \sum_{r \in R^w} f_r^w \right) \tag{3}$$

We can take the derivative of function (3) with respect to f_r^w using the chain rule, which yields:

$$\frac{\partial \mathrm{L}}{\partial f_r^w} = t_e(x_e) \delta_{e,r}^w - \lambda_r^w. \tag{4}$$

In order to ensure the success of the traffic assignment problem, it is essential that the KKT conditions are satisfied. These conditions encompass the following key points:

1. Primal feasibility: The decision variables must adhere to the constraints of the problem:

$$F^w - \sum_{r \in R^w} f_r^w \geq 0, \quad \forall w \in W, \quad f_r^w \geq 0, \quad \forall r \in R^w, w \in W \tag{5}$$

2. Dual feasibility: Lagrange multipliers must be non-negative:

$$\lambda_r^w \geq 0, \quad \forall r \in R^w, w \in W \tag{6}$$

3. Complementary slackness: The product of decision variables and their corresponding Lagrange multipliers must be zero:

$$\lambda_r^w \left(F^w - \sum_{r \in R^w} f_r^w \right) = 0, \quad \forall w \in W \tag{7}$$

4. Gradient of the Lagrangian (Stationary): The gradient of the Lagrangian function with respect to the decision variable f_r^w must be zero:

$$\frac{\partial \mathrm{L}}{\partial f_r^w} = t_e(x_e) \delta_{e,r}^w - \lambda_r^w = 0 \tag{8}$$

3. Lagrange Neural Network for Traffic Assignment as Nonlinear Optimization

This section will showcase the power of KKT conditions (4)- (8) in transforming the traffic assignment optimization problem (1) into a neural network using the Lagrange function (2). Our approach involves calculating the gradient of the Lagrange function for each variable and solving a set of differential equations using numerical methods. We are confident that we can prove that the equilibrium point of the obtained dynamic system provides the UE for the optimization problem (1).

Now, let's consider the primal variables as f_r^w, and λ_r^w as the Lagrange multipliers. We can express the gradient of the Lagrangian function (2) with respect to each variable, as follows:

$$\nabla_{f_r^w} \mathrm{L}(f, \lambda, \mu) = \frac{\partial \mathrm{L}}{\partial f_r^w} = t_e(x_e) \delta_{e,r}^w - \lambda_r^w \tag{9}$$

$$\nabla_{\lambda_r^w} \mathrm{L}(f, \lambda, \mu) = F^w - \sum_{r \in R^w} f_r^w \tag{10}$$

where ∇ denotes the gradient operator.

At t$t$he time, $f_r^w(t)$ represents the flow value for the route r and OD pair w. The dynamical system can be expressed using a gradient algorithm.

$$\frac{df_r^w}{dt} = -\frac{\partial \mathrm{L}}{\partial f_r^w} = -\left(t_e(x_e) \delta_{e,r}^w - \lambda_r^w \right) \tag{11}$$

$$\frac{d\lambda_w}{dt} = F^w - \sum_{r \in R^w} f_r^w \tag{12}$$

In order to maintain non-negative variable conditions within the system, we define the flow variable as $\max\{(f,\lambda),0\}$. The first equation (11) outlines the update rule for flow f_r^w, which is obtained by taking the negative derivative of the function (2). The second equation (12) presents the updated rules for the Lagrange multiplier λ_r^w. These dynamic equations are repeatedly applied to adjust the values of f_r^w λ_r^w and until they reach convergence.

Theorem 1: Suppose that (f^*, λ^*) is a stationary point of function (2), and that the Lagrangian function is positive definite and f^* is a regular point of the constrained optimization problem (1). Then, (f^*, λ^*) is an asymptotically stable point of neural network (11)-(12).

Proof: To prove that (f^*, λ^*) is an asymptotically stable point of neural network (11)- (12). We need to demonstrate that the system's dynamics converge to this point $t \to \infty$.

First, we observe that f^* is a stationary point of function (2), which implies (from KKT conditions) that $\nabla_f \mathrm{L}(f^*, \lambda^*) = 0$. By substituting the pre-definitional constraint $x_e = \sum_{w \in W} \sum_{r \in R^w} f_r^w \delta_{e,r}^w$, and Lagrange multiplier into equation (8), we obtain the following equation:

$$\begin{aligned}\frac{\partial \mathrm{L}}{\partial f_r^w} &= t_e\left(\sum_{w \in W}\sum_{r \in R^w} f_r^w \delta_{e,r}^w\right)\frac{\partial\left(\sum_{w \in W}\sum_{r \in R^w} f_r^w \delta_{e,r}^w\right)}{\partial f_r^w} - \lambda_r^w \\ &= t_e\left(\sum_{w \in W}\sum_{r \in R^w} f_r^w \delta_{e,r}^w\right)\delta_{e,r}^w - \lambda_r^w\end{aligned}$$

By using the equation mentioned earlier, we can find the UE for the optimization problem (1). From the KKT conditions (5)- (8), we obtain $t_e\left(\sum_{w \in W}\sum_{r \in R^w} f_r^w \delta_{e,r}^w\right)\delta_{e,r}^w - \lambda_r^w = 0 \Rightarrow \lambda_r^w = t_e\left(\sum_{w \in W}\sum_{r \in R^w} f_r^w \delta_{e,r}^w\right)\delta_{e,r}^w$.

Here, since $f_r^w \geq 0$, $\lambda_r^w \geq 0$ and then, complementary slackness condition from (7) must be either $\lambda_r^w = 0$ or $\left(F^w - \sum_{r \in R^w} f_r^w\right) = 0$. In this way, the UE of the problem (1) is obtained as:

$$UE = \begin{cases} t_e\left(\sum_{w \in W}\sum_{r \in R^w} f_r^w \delta_{e,r}^w\right)\delta_{e,r}^w, & \lambda_r^w = 0 \\ t_e\left(\sum_{w \in W}\sum_{r \in R^w} f_r^w \delta_{e,r}^w\right)\delta_{e,r}^w - \lambda_r^w, & \lambda_r^w > 0 \end{cases}$$

If the above KKT conditions for the traffic assignment problem are met by (f^*, λ^*), then the equation provides a valid solution. Moving on to the neural network's dynamics, we can use the update rules to rephrase equations (11) and (12) for f_r^w λ_r^w and. Linearizing the equation system around a point (f^*, λ^*) involves computing the Jacobian matrix.

$$J=\begin{bmatrix} -\frac{\partial}{\partial f_r^w}\left(-\left(t_e(\sum_{w\in W}\sum_{r\in R^w} f_r^w\delta_{e,r}^w)\delta_{e,r}^w-\lambda_r^w\right)\right) & 0 \\ \frac{\partial}{\partial f_r^w}\left(F^w-\sum_{r\in R^w} f_r^w\right) & 0 \end{bmatrix}_{(f^*,\lambda^*)}$$

Since f^* is a regular point of the constrained optimization problem (1), it can be deduced that the Hessian matrix of the Lagrangian is positive definite at f^*. Therefore, it follows that the Jacobian matrix J is negative definite at (f^*,λ^*). By applying the Hartman-Grobman theorem, it can be determined that the system dynamics in the vicinity of (f^*,λ^*) are locally equivalent to those of a linearized system. Given that J is negative definite, the linearized system is asymptotically stable at (f^*,λ^*). Thus, it can be concluded that the original nonlinear system dynamics are also asymptotically stable at (f^*,λ^*). The proof is now complete.

3.1. Stability of The Dynamical System

Lyapunov's method is a powerful tool that allows us to analyze the stability of dynamical systems. However, in order to use this method effectively, it is essential to find an appropriate Lyapunov function, which can be a challenging task. To implement Lyapunov's method and show that it is a reliable tool, we need to find a Lyapunov function $V(f,\lambda)$ that is positive definite and has a negative definite derivative along the trajectories of the dynamical system.

One possible Lyapunov function for neural network (11)- (12) is:

$$V(f,\lambda)=\frac{1}{2}\sum_{w\in W}\sum_{r\in R}\left|\left(\frac{\partial \mathrm{L}(f,\lambda)}{\partial f_r^w}\right)\right|^2+\frac{1}{2}\left|\left(\sum_{w\in W}\left(\sum_{r\in R^w}(F^w-f_r^w)\right)\right)\right|^2 \tag{13}$$

To demonstrate that $V(f,\lambda)$ is indeed a Lyapunov function, we must verify that it satisfies the two necessary conditions:

1. $V(f,\lambda)\geq 0$ for all (f,λ), and $V(f,\lambda)=0$ only at (f,λ).
2. $\frac{dV}{dt}\leq 0$ for all f λ. and.

It is evident that the first condition is met as both terms $V(f,\lambda)$ are non-negative. Furthermore, $V(f,\lambda)=0$ only when both terms are zero. The first term equals zero if and only if $\frac{\partial L(f,\lambda)}{\partial f_r^w}=0$ for all $r\in R$ $w\in W$ and, which indicates that (f,λ) is a stationary point of the system. The second term equals zero if and only if $\sum_{w\in W}\left(\sum_{r\in R^w}(F^w-f_r^w)\right)=0$, which implies that the flow conservation constraint is met. To establish the second condition, we must differentiate $V(f,\lambda)$ with respect to time and demonstrate that it is negative or zero. We obtain:

$$\frac{dV}{dt}=\sum_{w\in W}\sum_{r\in R}\left(\frac{\partial V}{\partial f_r^w}\frac{df_r^w}{dt}\right)+\frac{\partial V}{\partial \lambda}\frac{d\lambda}{dt}=-\sum_{w\in W}\sum_{r\in R}\left|\frac{\partial L(f,\lambda)}{\partial f_r^w}\right|^2+\left|\sum_{w\in W}\left(\sum_{r\in R^w}(F^w-f_r^w)\right)\right|^2\leq 0$$

The last inequality follows from the Cauchy-Schwarz inequality, which states that $|\langle u,v\rangle|^2 \leq |u|^2|v|^2$ any vector $u\ v.V(f,\lambda)$, is a Lyapunov function for the neural network, which implies that the stationary point (f,λ) is stable.

Through the usage of the Cauchy-Schwarz inequality, which guarantees that $|\langle u,v\rangle|^2 \leq |u|^2|v|^2$ for all vectors $u\ v$, we can conclusively prove the validity of the aforementioned inequality. This, in turn, confirms that $V(f,\lambda)$ is a Lyapunov function for the neural network, providing affirmation of the stability of the stationary point (f,λ). Therefore, we have successfully demonstrated the effectiveness of Lyapunov's method in evaluating the stability of the given dynamical system. Furthermore, we have established a Lyapunov function that solidifies the stability of the system at the origin.

To solve the above dynamical system using Euler's method, we need to discretize the system in time. Let Δt be the time step. Then, we can approximate the derivatives by finite differences:

$$\frac{df_r^w}{dt} \approx \frac{f_{r,n+1}^w - f_{r,n}^w}{\Delta t}, \qquad \frac{d\lambda_r^w}{dt} \approx \frac{\lambda_{r,n+1}^w - \lambda_{r,n}^w}{\Delta t} \tag{14}$$

where $f_{r,n}^w$, and $\lambda_{r,n}^w$, denote the values of $f_r^w\ \lambda_{r,n}^w$ and at time step n. Substituting these approximations into the dynamical system, we get:

$$\frac{f_{r,n+1}^w - f_{r,n}^w}{\Delta t} = -\frac{\partial \mathrm{L}}{\partial f_r^w} = -\left[t_e \left(\sum_{w\in W} \sum_{r\in R^w} f_{r,n}^w \delta_{e,r}^w \right) \delta_{e,r}^w - \lambda_{r,n}^w \right] \tag{15}$$

$$\frac{\lambda_{r,n+1}^w - \lambda_{r,n}^w}{\Delta t} = F^w - \sum_{r\in R^w} f_{r,n}^w \tag{16}$$

Solving for $f_{r,n+1}^w$ and $\lambda_{r,n+1}^w$, we get:

$$f_{r,n+1}^w = f_{r,n}^w - \Delta t \left[t_e \left(\sum_{w\in W} \sum_{r\in R^w} f_{r,n}^w \delta_{e,r}^w \right) \delta_{e,r}^w + \lambda_{r,n}^w \right] \tag{17}$$

$$\lambda_{r,n+1}^w = \lambda_{r,n}^w + \Delta t (F^w - \sum_{r\in R^w} f_{r,n}^w) \tag{18}$$

In order to ensure that all variables are non-negative, the system is reformulated as follows:

$$f_{r,n+1}^w = \max\left\{ f_{r,n}^w - \Delta t \left[t_e \left(\sum_{w\in W} \sum_{r\in R^w} f_{r,n}^w \delta_{e,r}^w \right) \delta_{e,r}^w + \lambda_{r,n}^w \right], 0 \right\} \tag{19}$$

$$\lambda_{r,n+1}^w = \max\left\{ \lambda_{r,n}^w + \Delta t (F^w - \sum_{r\in R^w} f_{r,n}^w), 0 \right\} \tag{20}$$

These equations give us a way to update values of f_r^w and λ_r^w at each time step $n+1$ based on their values at the previous time step n. To start the iteration, we need to initialize these variables at the time step $n=0$. Let $f_{r,0}^w\ \lambda_{r,0}^w$ and denote their initial values. Then, we can use the following algorithm to solve the dynamical system using Euler's method:

1. Set $n=0$ and initialize $f_{r,n}^w = f_{r,0}^w\ \lambda_{r,n}^w = \lambda_{r,0}^w$, for all $r \in R^w$ and $w \in W$.
2. Set the time step Δt.
3. For $n = 0,1,2,\ldots,$ do the following:
    a. Compute $f_{r,n+1}^w$ and $\lambda_{r,n+1}^w$ use the updated equations above.

b. Set $f_{r,n}^{w} = f_{r,n+1}^{w}$ and $\lambda_{r,n}^{w} = \lambda_{r,n+1}^{w}$ for all $r \in R^{w}$ $w \in W$ and.

c. Increment n and repeat step 3.

This algorithm will iteratively update the values of f_{r}^{w} and λ_{r}^{w} at each time step until convergence. The convergence criteria can vary depending on the specific problem and implementation, but a common one is to stop the iteration when the change in the objective function value or the norm of the gradient falls below a certain threshold.

4. A Numerical Example

In this section, we provide a numerical example to illustrate the computation of traffic flow within a network, based on demand and travel time functions. Consider the network depicted in Figure 1. The travel time for each edge is defined as a function of the flow on that edge, denoted as x_e given by $t(x_e) = 1 + 0.15x_e$.

We have two OD pairs, namely (1,5) and (2,5), with demand values of $F^{1,5} = 20$ $F^{2,5} = 30$ and respectively. To determine the traffic flow, we must account for all potential routes between these OD pairs. For OD pair (1,5), the set of all feasible routes is defined as $R^{1,5} = [(1,3,5),(1,4,5)]$, and for OD pair (2,5), it is defined as $R^{2,5} = [(2,3,5),(2,4,5)]$. Each route is represented as a sequence of nodes.

Subsequently, we can calculate the objective function for the traffic assignment problem as follows:

$$\begin{aligned}\sum_{e\in E}\int_0^{x_e(f)} t_e(u)du &= \int_0^{x_{(1,3)}(f)} t_{(1,3)}(u)du + \int_0^{x_{(3,5)}(f)} t_{(3,5)}(u)du + \int_0^{x_{(1,4)}(f)} t_{(1,4)}(u)du + \int_0^{x_{(4,5)}(f)} t_{(4,5)}(u)du \\ &+ \int_0^{x_{(2,3)}(f)} t_{(2,3)}(u)du + \int_0^{x_{(2,4)}(f)} t_{(2,4)}(u)du + \int_0^{x_{(3,5)}(f)} t_{(3,5)}(u)du + \int_0^{x_{(4,5)}(f)} t_{(4,5)}(u)du \\ &= \int_0^{x_{(1,3)}(f)} (1+0.15u)du + \int_0^{x_{(3,5)}(f)} (1+0.15u)du + \int_0^{x_{(1,4)}(f)} (1+0.15u)du + \int_0^{x_{(4,5)}(f)} (1+0.15u)du \\ &+ \int_0^{x_{(2,3)}(f)} (1+0.15u)du + \int_0^{x_{(2,4)}(f)} (1+0.15u)du + \int_0^{x_{(3,5)}(f)} (1+0.15u)du + \int_0^{x_{(4,5)}(f)} (1+0.15u)du\end{aligned} \tag{21}$$

where $x_e(f)$ is the flow on edge e, and $t_e(u) = 1 + 0.15u$ is the travel time function for edge e.

For each node w in the network, the total flow into the node must equal the total flow out of the node. In other words, the demand for each OD pair must be met by the traffic flows on the network. The flow conservation constraint is given by:

$$\text{For OD pair } (1,5): \; f_{(1,3,5)}^{(1,5)} + f_{(1,4,5)}^{(1,5)} = 20; \;\; \text{For OD pair } (2,5): \; f_{(2,3,5)}^{(2,5)} + f_{(2,4,5)}^{(2,5)} = 30$$

The traffic flow on each route must be non-negative. The non-negative flow constraint is given by:

$$f_{(1,3,5)}^{(1,5)} \geq 0,\; f_{(1,4,5)}^{(1,5)} \geq 0,\; f_{(2,3,5)}^{(2,5)} \geq 0,\; f_{(2,4,5)}^{(2,5)} \geq 0$$

To calculate these constraints, we need to determine which routes use each edge. Based on the definitions given in the problem statement, we can obtain that:

- Edge (1,3) is used by route (1,3,5) in $R^{(1,5)}; x_{(1,3)} = f_{(1,3,5)}^{(1,5)}$
- Edge (1,4) is used by route (1,4,5) in $R^{(1,5)}; x_{(1,4)} = f_{(1,4,5)}^{(1,5)}$.
- Edge (2,3) is used by route (2,3,5) in $R^{(2,5)}; x_{(2,3)} = f_{(2,3,5)}^{(2,5)}$.
- Edge (2,4) is used by route (2,4,5) in $R^{(2,5)}; x_{(2,4)} = f_{(2,4,5)}^{(2,5)}$.

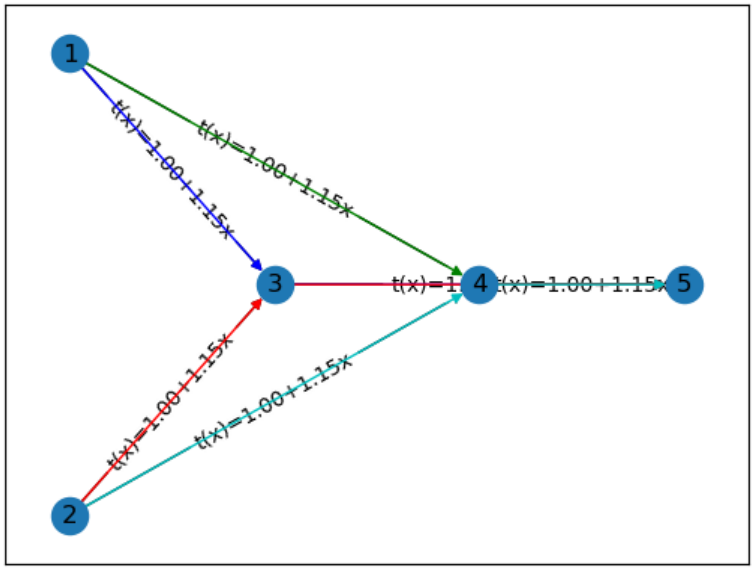

Figure 1. Network for the given problem with routes

Using these values, an optimization problem equivalent to problem (1) can be obtained as follows:

$$\begin{aligned} \min_{f} \quad & \left(f^{(1,5)}_{(1,3,5)} + f^{(1,5)}_{(1,4,5)} + f^{(2,5)}_{(2,3,5)} + f^{(2,5)}_{(2,4,5)} + 0.075\left((f^{(1,5)}_{(1,3,5)})^2 + (f^{(1,5)}_{(1,4,5)})^2 + (f^{(2,5)}_{(2,3,5)})^2 + (f^{(2,5)}_{(2,4,5)})^2 \right) \right) \\ \text{s.t.} \quad & f^{(1,5)}_{(1,3,5)} + f^{(1,5)}_{(1,4,5)} = 20 \\ & f^{(2,5)}_{(2,3,5)} + f^{(2,5)}_{(2,4,5)} = 30 \\ & f^{(1,5)}_{(1,3,5)} \geq 0,\ f^{(1,5)}_{(1,4,5)} \geq 0,\ f^{(2,5)}_{(2,3,5)} \geq 0,\ f^{(2,5)}_{(2,4,5)} \geq 0 \end{aligned} \tag{22}$$

For this problem, the Lagrange function equivalent to function (2) is obtained as follows:

$$\begin{aligned} L(f, \lambda_1, \lambda_2) = {} & f^{(1,5)}_{(1,3,5)} + f^{(1,5)}_{(1,4,5)} + f^{(2,5)}_{(2,3,5)} + f^{(2,5)}_{(2,4,5)} + 0.075\left((f^{(1,5)}_{(1,3,5)})^2 + (f^{(1,5)}_{(1,4,5)})^2 + (f^{(2,5)}_{(2,3,5)})^2 + (f^{(2,5)}_{(2,4,5)})^2 \right) \\ & + \lambda_1 (20 - f^{(1,5)}_{(1,3,5)} - f^{(1,5)}_{(1,4,5)}) + \lambda_2 (30 - f^{(2,5)}_{(2,3,5)} - f^{(2,5)}_{(2,4,5)}) \end{aligned} \tag{23}$$

where λ_1 λ_2 and are the Lagrange multipliers.

After calculating the derivative of the Lagrange function with respect to each variable f and λ, we have a dynamical system that includes a system of differential equations that corresponds to equations (11)-(12).

The derivative for function (23) with respect to f and λ are as follows:

$$\begin{aligned} & \frac{\partial L}{\partial f^{(1,5)}_{(1,3,5)}} = 1 + 0.15 f^{(1,5)}_{(1,3,5)} - \lambda_1 = 0 \qquad \frac{\partial L}{\partial f^{(1,5)}_{(1,4,5)}} = 1 + 0.15 f^{(1,5)}_{(1,4,5)} - \lambda_1 = 0 \\ & \frac{\partial L}{\partial f^{(2,5)}_{(2,3,5)}} = 1 + 0.15 f^{(2,5)}_{(2,3,5)} - \lambda_2 = 0 \qquad \frac{\partial L}{\partial f^{(2,5)}_{(2,4,5)}} = 1 + 0.15 f^{(2,5)}_{(2,4,5)} - \lambda_2 = 0 \\ & \frac{\partial L}{\partial \lambda_1} = 20 - f^{(1,5)}_{(1,3,5)} - f^{(1,5)}_{(1,4,5)} = 0 \qquad \frac{\partial L}{\partial \lambda_2} = 30 - f^{(2,5)}_{(2,3,5)} - f^{(2,5)}_{(2,4,5)} = 0 \end{aligned} \tag{24}$$

Then, the dynamical system is obtained as:

$$\frac{\partial f_{(1,3,5)}^{(1,5)}}{\partial t} = -\left(1+0.15 f_{(1,3,5)}^{(1,5)} - \lambda_1\right) \qquad \frac{\partial f_{(1,4,5)}^{(1,5)}}{\partial t} = -\left(1+0.15 f_{(1,4,5)}^{(1,5)} - \lambda_1\right)$$
$$\frac{\partial f_{(2,3,5)}^{(2,5)}}{\partial t} = -\left(1+0.15 f_{(2,3,5)}^{(2,5)} - \lambda_2\right) \qquad \frac{\partial f_{(2,4,5)}^{(2,5)}}{\partial t} = -\left(1+0.15 f_{(2,4,5)}^{(2,5)} - \lambda_2\right) \qquad (25)$$
$$\frac{\partial \lambda_1}{\partial t} = 20 - f_{(1,3,5)}^{(1,5)} - f_{(1,4,5)}^{(1,5)} \qquad \frac{\partial \lambda_2}{\partial t} = 30 - f_{(2,3,5)}^{(2,5)} - f_{(2,4,5)}^{(2,5)}$$

where all variables are accepted as: $\max\left\{\left(f,\lambda\right),0\right\}$.

In order to apply Euler's method (equations (14) to (20)) in the Python 3.0 program, we need to establish the initial conditions and select an appropriate step size.

Let us suppose the initial time points to be denoted as follows:

$$f_{(1,3,5)}^{(1,5)} = 0,\ f_{(1,4,5)}^{(1,5)} = 0,\ f_{(2,3,5)}^{(2,5)} = 0,\ f_{(2,4,5)}^{(2,5)} = 0, \lambda_1 = 0, \lambda_2 = 0$$

A step size of 0.01 may be selected for this computational process. Subsequently, Euler's method can be applied iteratively to update values and Lagrange multipliers. The updated rules are delineated as follows:

$$f_{(1,3,5)}^{(1,5)}(t+\Delta t) = \max\left\{ f_{(1,3,5)}^{(1,5)}(t) - \Delta t \cdot \left(1+0.15 f_{(1,3,5)}^{(1,5)}(t) - \lambda_1\right), 0\right\}$$
$$f_{(1,4,5)}^{(1,5)}(t+\Delta t) = \max\left\{ f_{(1,4,5)}^{(1,5)}(t) + \Delta t \cdot \left(1+0.15 f_{(1,4,5)}^{(1,5)}(t) - \lambda_1\right), 0\right\}$$
$$f_{(2,3,5)}^{(2,5)}(t+\Delta t) = \max\left\{ f_{(2,3,5)}^{(2,5)}(t) + \Delta t \cdot \left(1+0.15 f_{(2,3,5)}^{(2,5)}(t) - \lambda_2\right), 0\right\}$$
$$f_{(2,4,5)}^{(2,5)}(t+\Delta t) = \max\left\{ f_{(2,4,5)}^{(2,5)}(t) - \Delta t \cdot \left(1+0.15 f_{(2,4,5)}^{(2,5)}(t) - \lambda_2\right), 0\right\}$$
$$\lambda_1(t+\Delta t) = \max\left\{\lambda_1(t) + \Delta t \cdot \left(20 - f_{(1,3,5)}^{(1,5)}(t) - f_{(1,4,5)}^{(1,5)}(t)\right), 0\right\}$$
$$\lambda_2(t+\Delta t) = \max\ \left\{\lambda_2(t) + \Delta t \cdot \left(30 - f_{(2,3,5)}^{(2,5)}(t) - f_{(2,4,5)}^{(2,5)}(t)\right), 0\right\}$$

Thus the results obtained after 1000 iterations are as follows: $f_{(1,3,5)}^{(1,5)} = 9.34,\ f_{(1,4,5)}^{(1,5)} = 9.34,$ $f_{(2,3,5)}^{(2,5)} = 14.84,\ f_{(2,4,5)}^{(2,5)} = 14.84,\ \lambda_1 = 0.88,\ \lambda_2 = 0.82.$

Accordingly, the time-dependent changes of flows on each route and Lagrange multipliers along the route are presented in Figure II.

In order to calculate the minimum total travel time, we can substitute values of $f_{(1,3,5)}^{(1,5)}, f_{(1,4,5)}^{(1,5)}, f_{(2,3,5)}^{(2,5)},$ $f_{(2,4,5)}^{(2,5)}$ and into an objective function (22) and then minimize it. That is, by substituting these values into an objective function (22), we have 94.48.

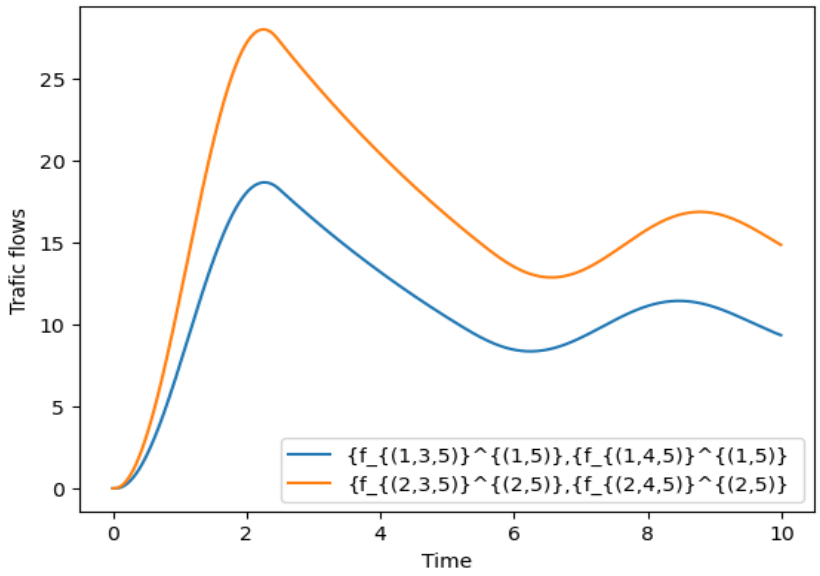

Figure 2. The traffic flow over time

In light of Theorem 1, it has been established that the outcomes derived are representative of the asymptotically stable points within the neural network framework (Equations (11) and (12)). Moreover, these outcomes not only meet the stringent KKT conditions but also fulfill the requirements for the optimization problem outlined in problem (22). Consequently, they constitute the UE of said optimization problem (22).

It is pertinent to note that the utilization of the Frank-Wolfe algorithm yields a solution with a numerical value of 98.75, while the application of the Lagrange neural network model employing the Euler approach results in a solution value of 94.48.

The fundamental goal of this research is to discover the best route preferences for each user in the network. As a result, when the acquired results are compared, it is discovered that the approach provided in this article produces more effective results for the optimization model of classical traffic assignment problems and converges towards UE.

5. Conclusions

This article explored a model for optimizing traffic assignment within a network. It began by establishing the Lagrange function to comprehend the optimal conditions of the static traffic assignment model. The Lagrange function assisted in illustrating the existence of points adhering to the Karush-Kuhn-Tucker conditions. Subsequently, it elucidated how the Lagrange function could be transformed into a dynamic system employing the gradient method. It was mathematically proven that the points derived from this system converged towards the UE points, and further details were provided regarding the asymptotic and Lyapunov stability of the resulting system. A neural network model was also applied to a numerical example, and the Euler method was employed to solve the dynamic system. Finally, the temporal evolution of traffic in the network routes was visually represented using a graphical illustration. Furthermore, the results obtained through the Frank Wolfe algorithm and the methodology presented in this study were compared, with our findings confirming the superior efficacy of the approach proposed herein.

It is important to note that this solution method particularly entails a higher computational workload, as well as a greater demand for storage space, especially in the case of large and intricate networks. However, despite all these associated costs, upon system implementation, it is possible to achieve superior and more reliable results compared to existing methods.

In the future, further research in this field is likely to hold significant potential for advancing our understanding of network traffic allocation and optimization, as well as for developing practical applications. Moreover, this solution process can be seamlessly integrated into network traffic assignment problems, including those that involve analyzing traffic congestion within the network.

Ethical statement:

The author declares that this document does not require ethics committee approval or any special permission. The study does not cause any harm to the environment and does not involve the use of animal or human subjects.

Conflict of interest:

The author claims that he has no conflicts of interest.

Authors' Contributions:

The author made a substantial contribution to the paper's authoring. The final manuscript was read and approved by the author.

References

[1] J.G. Wardrop, "Some theoretical aspects of road traffic research," Proceedings of the Institution of Civil Engineers, Part II, vol. 1, no. 3, pp. 325-378, 1952.

[2] M. Frank and P. Wolfe, "An algorithm for quadratic programming," Naval Research Logistics Quarterly, vol. 3, no. 1-2, pp. 95-110, 1956.

[3] Y. Sheffi and W. B. Powell, "A survey of transportation network models," Transportation Research Part B: Methodological, vol. 19, no. 5, pp. 381-391, 1985.

[4] C. F. Daganzo and Y. Sheffi, "On stochastic models of traffic assignment," Transportation Science, vol. 11, no. 3, pp. 253-274, 1977.

[5] M. Beckmann, C. B. McGuire, and C. B. Winsten, "Studies in the economics of transportation," Yale University Press, 1956.

[6] S. Kirkpatrick, C. D. Gelatt, and M. P. Vecchi, "Optimization by simulated annealing," Science, vol. 220, no. 4598, pp. 671-680, 1983.

[7] M. J. Smith and P. J. Wieskamp, "The network design problem: Dual and primal methods," Transportation Research Part B: Methodological, vol. 13, no. 1, pp. 1-16, 1979.

[8] M. Florian and S. Nguyen, "An efficient algorithm for the continuous network design problem," Transportation Science, vol. 18, no. 3, pp. 269-291, 1984.

[9] S. Peeta and A. K. Ziliaskopoulos, "Foundations of dynamic traffic assignment: the past, the present and the future," Networks and Spatial Economics, vol. 1, no. 3-4, pp. 233-265, 2001.

[10] A. Sumalee and W. H. Lam, "Traffic congestion modeling: A state-of-the-art review," Transportation Research Part C: Emerging Technologies, vol. 14, no. 2, pp. 89-123, 2006.

[11] H. Jin, L. Sun, X. Wang, and Y. Wang, "Simulation-based dynamic traffic assignment algorithm considering driver routing behavior," Transportation Research Part C: Emerging Technologies, vol. 86, pp. 245-264, 2018.

[12] J. Lin, B. Yu, H. Huang, S. Wang, and M. Zhou, "A bilevel optimization model for sustainable transportation planning with consideration of driver compliance behavior," Transportation Research Part D: Transport and Environment, vol. 76, pp. 161-180, 2019.

[13] X. Hu, C. Chen, and Y. Jiang, "A network loading model with uncertain flow and travel time for sustainable urban transport," Transportation Research Part C: Emerging Technologies, vol. 112, pp. 63-81, 2020.

[14] W. Xie, Y. Liu, H. Huang, and Z. Gao, "A data assimilation augmented Wolfe dual method for dynamic traffic assignment," Transportation Research Part C: Emerging Technologies, vol. 111, pp. 463-486, 2020.

[15] Y. Li, J. Wu, B. Yang, and F. Peng, "A variable-penalty augmented Lagrangian method for large-scale traffic assignment," Transportation Research Part B: Methodological, vol. 149, pp. 305-326, 2021.

[16] A. Krylatov, "Optimization Models and Methods for Equilibrium Traffic Assignment," Transportation Research Procedia, vol. 40, pp. 166-173, 2019.

[17] S. Zhang and A. G. Constantinides, "Lagrange Programming Neural Networks," IEEE Transactions on Circuits and Systems II: Analog and Digital Signal Processing, vol. 39, no. 7, pp. 441-452, Jul. 1992.

[18] Y. Leung, K.Z. Chen, Y.C. Jiao, X.B. Gao and K.S. Leung, "A new gradient-based neural network for solving linear and quadratic programming problems," IEEE Transactions on Neural Networks, vol. 12, no. 5, pp. 1074-1083, 2001.

[19] K. M. Lee, Y. J. Park and J. H. Kim, "A Lagrange programming neural network for large-scale convex programming problems," Neurocomputing, vol. 115, pp. 109-117, 2013.

[20] Y. Liu, G. Li and J. Li, "Lagrange programming neural network for solving non-linear programming problems," Neurocomputing, vol. 275, pp. 1156-1165, 2018.

[21] S. C. Dafermos and F. T. Sparrow, "The traffic assignment problem for a general network," J. Res. Natl. Bur. Stand. B, vol. 73, no. 2, pp. 91-118, 1969.

[22] T. L. Friesz and D. Bernstein, "Foundations of Network Optimization and Games," New York, NY: Springer, 2016.

[23] M. Patriksson, "The Traffic Assignment Problem: Models and Methods," Courier Dover Publications, New York, 2015.

[24] A. T. Karaşahin ve A. E. Tümer, "Real-time traffic signal timing approach based on artificial neural network," MANAS Journal of Engineering, vol. 8, no. 1, pp. 49-54, 2020.

[25] Q. Zhang, S.Q. Liu, ve M. Masoud, "A traffic congestion analysis by user equilibrium and system optimum with incomplete information," Journal of Combinatorial Optimization, vol. 43, no:1, pp. 1391–1404, 2022.

[26] B. Javani and A. Babazadeh, "Origin-destination-based truncated quadratic programming algorithm for traffic assignment problem," Transportation Letters, vol. 9, no. 3, pp. 166-176, 2017.

[27] A. Babazadeh, B. Javani, G. Gentile, and M. Florian, "Reduced gradient algorithm for user equilibrium traffic assignment problem," Transportmetrica A: Transport Science, vol. 16, no. 3, pp. 1111-1135, 2020.

[28] V. Morandi, "Bridging the user equilibrium and the system optimum in static traffic assignment: a review," 4OR-Q J Oper Res, 2023, doi: 10.1007/s10288-023-00540-w.

Middle East Journal of Science

https://dergipark.org.tr/mejs **MEJS**

e-ISSN:2618-6136

Research Article

ON ρ −STATISTICAL CONVERGENCE OF ORDER (α,β) FOR SEQUENCES OF FUZZY NUMBERS

Damla BARLAK*

Dicle University, Faculty of Science, Department of Statistics, 21280, Diyarbakır, Turkey
* Corresponding author; dyagdiran@hotmail.com

Abstract: *In this study, we first give the definition of ρ −statistical convergence of order (α,β) for sequences of fuzzy numbers. We also define the strongly $w(\rho,F,q)$ −summable of order (α,β) and the strongly $w(\rho,F,q,f)$ −summable of order (α,β), defined by a modulus function f for sequences of fuzzy numbers. Later we give some inclusion theorems between these sets and the set $S_\alpha^\beta(\rho,F)$.*

Keywords*: Modulus function, Sequence of fuzzy numbers, Statistical convergence.*

Received: July 12, 2023 *Accepted: October 5, 2023*

1. Introduction

The concept of statistical convergence was independently defined by Fast [1] and Steinhaus [2] in 1951. Schoenberg [3] redefined the concept of statistical convergence and provided some of its properties. Subsequently, statistical convergence has been used by many researchers in statistical measurement theory, summability theory, Banach spaces, trigonometric series, and fuzzy set theory. Several researchers, including ([4]- [7]) , have conducted studies on this concept.

Zadeh [8] first introduced fuzzy set theory. Matloka [9] provided the definition of fuzzy number sequences and defined the concepts of boundedness and convergence of sequences of fuzzy numbers, along with some properties. He showed that many properties valid for real number sequences also hold for sequences of fuzzy numbers. Since then, numerous studies have been conducted and continue to be conducted on sequences of fuzzy numbers.

The concept of statistical convergence for sequences of fuzzy numbers was introduced by Nuray & Savaş [10]. Nuray & Savaş [10] and Kwon [11] examined the relationship between statistical convergence, convergence, lacunary statistical convergence, and strong Cesàro convergence for sequences of fuzzy numbers.

The degree of statistical convergence of a sequence was provided by Gadjiev & Orhan [12]. Subsequently, the idea of statistical convergence of order α and strong p-Cesàro summability of order α was proposed by Çolak [13]. Statistical convergence of order (α, β) was first defined by Şengül [14]. Altınok & Et [15] introduced the definition of statistical convergence of order (β,γ) for sequences of fuzzy numbers.

Çakallı [16] defined ρ-statistical convergence in real number sequences. Subsequently, several researchers, including ([17]- [22]) , have conducted studies on this topic. The aim of this study is to generalize Aral's work [17] on real number sequences to sequences of fuzzy number.

2. Definitions and Preliminaries

In this section, we have discussed the fundamental concepts that we will use throughout this study.

A fuzzy number is a fuzzy set that maps from the real numbers $\mathbb{R}$ to the closed interval [0,1], satisfying the following properties:

(i) Z is normal, which means there exists $z_0 \in \mathbb{R}$ such that $Z(z_0) = 1$.

(ii) Z is fuzzy convex, which means for $z, t \in \mathbb{R}$ and $0 \leq \beta \leq 1$, we have $Z(\beta z + (1-\beta)t) \geq \min[Z(z), Z(t)]$.

(iii) Z is upper semi-continuous.

(iv) The support of Z, denoted by suppZ, is defined as the closure of the set {z∈R:Z(z)>0}, which is a compact set.

An α-level set of a fuzzy number, denoted as $[Z]^\alpha$, is defined as follows:

$$[Z]^\alpha = \begin{cases} \{z \in \mathbb{R}: Z(z) \geq \alpha\}, & if\ \alpha \in (0,1], \\ \text{supp}Z, & if\ \alpha = 0. \end{cases}$$

For a number Z to be a fuzzy number, the necessary and sufficient condition is that for each $\alpha \in [0,1]$, the set $[Z]^\alpha$ is a closed interval, and $[Z]^1 \neq \emptyset$ is obvious. We will denote the space of all fuzzy numbers with real terms as $L(\mathbb{R})$.

The distance between fuzzy numbers Z and T is calculated using the metric:

$$d(Z,T) = \sup_{0 \leq \alpha \leq 1} d_H([Z]^\alpha, [T]^\alpha)$$

where d_H is the Hausdorff metric and for $Z^\alpha = [\underline{Z}^\alpha, \bar{Z}^\alpha]$ and $T^\alpha = [\underline{T}^\alpha, \bar{T}^\alpha]$, it is defined as:

$$d_H([Z]^\alpha, [T]^\alpha) = \max\{|\underline{Z}^\alpha - \underline{T}^\alpha|, |\bar{Z}^\alpha - \bar{T}^\alpha|\}.$$

The distance d is a metric on $L(\mathbb{R})$ and it is complete.

A sequence $Z = (Z_k)$ of fuzzy number is a function Z from the set $\mathbb{N}$ of all natural numbers into $L(\mathbb{R})$ that is $Z: \mathbb{N} \to L(\mathbb{R})$ [9]. In this case, each term of the sequence (Z_k) corresponds to a fuzzy number.

A sequence $Z = (Z_k)$ of fuzzy numbers is said to be statistically convergent to a fuzzy number Z_0 if for every $\varepsilon > 0$,

$$\lim_{n \to \infty} \frac{1}{n} |\{k \leq n: d(Z_k, Z_0) \geq \varepsilon\}| = 0.$$

where the vertical bars indicate the number of elements in the enclosed set. We denote the set of all statistically convergent sequences of fuzzy numbers as $S(F)$.

The (α, β) natural density of a subset E, which is a subset of the set of natural numbers $\mathbb{N}$, is defined as follows:

$$\delta_\alpha^\beta(E) = \lim_n \frac{1}{n^\alpha} |\{k \leq n: k \in E\}|^\beta.$$

Here, the expression $|\{k \leq n: k \in E\}|^\beta$ represents the β power of the number of elements in E that are not greater than n.

Let $Z = (Z_k)$ be a sequence of fuzzy numbers and $0 < \alpha \leq \beta \leq 1$. If for every $\varepsilon > 0$, there exists a fuzzy number Z_0 such that

$$\lim_{n \to \infty} \frac{1}{n^\alpha} |\{k \leq n: d(Z_k, Z_0) \geq \varepsilon\}|^\beta = 0$$

the sequence $Z = (Z_k)$ is said to be statistically convergent of order (α, β) to the fuzzy number Z_0.

Let $Z = (Z_k)$ be a sequence of points in the fuzzy number set $L(\mathbb{R})$ and $0 < \alpha \leq 1$. If for every $\varepsilon > 0$, there exists a fuzzy number Z_0 such that

$$\lim_{n \to \infty} \frac{1}{\rho_n^\alpha} |\{k \leq n: d(Z_k, Z_0) \geq \varepsilon\}| = 0$$

the sequence $Z = (Z_k)$ is said to be ρ −statistically convergent of order α to the fuzzy number Z_0. Here, $\rho = (\rho_n)$ is an non-decreasing sequence of positive real numbers that approaches to ∞, satisfying $\limsup_{n\to\infty} \frac{\rho_n^\alpha}{n} < \infty$, $\Delta\rho_n^\alpha = O(1)$ and $\Delta Z_n^\alpha = Z_{n+1}^\alpha - Z_n^\alpha$ for every positive integer n. In this case, it is denoted as $S_\rho^\alpha(F) - \lim Z_k = Z_0$.

If $\rho = (\rho_n) = n$ and $\alpha = 1$, there is no difference between ρ −statistical convergence of order α and statistical convergence.

Throughout this study, let $\rho = (\rho_n)$ be a sequence as given above.

The concept of modulus function was first introduced by Nakano [23]. If a function $f: [0,\infty) \to [0,\infty)$ satisfies the following properties:

(i) $f(x) = 0$ if and only if $x = 0$,

(ii) for every $x, y \geq 0$, $f(x+y) \leq f(x) + f(y)$,

(iii) f is right-continuous at , $x = 0$,

(iv) f is increasing, then f is called a modulus function.

Let (p_k) be a positive and bounded real number sequence with $\sup_k p_k = N$. Let $K = max(1, 2^{N-1})$ and $a_k, b_k \in \mathbb{C}$. The inequality

$$|a_k + b_k|^{p_k} \leq K(|a_k|^{p_k} + |b_k|^{p_k}) \qquad (1)$$

given by Maddox [24] will be used throughout this study.

3. Main Results

In this section, we first introduced definition of ρ −statistically convergent of order (α, β) definition for sequences of fuzzy numbers. We also defined the sets of strongly $w_\alpha^\beta(\rho, F, q)$ −summable sequences and strongly $w_\alpha^\beta(\rho, F, q, f)$ −summable sequences with respect to the modulus function f. Furthermore, we provided some inclusion theorems between these sets and the set $S_\alpha^\beta(\rho, F)$.

Definition 3.1. Let $Z = (Z_k)$ be a sequence of fuzzy numbers and $0 < \alpha \leq \beta \leq 1$. If there exists a fuzzy number Z_0 such that

$$\lim_{n\to\infty} \frac{1}{\rho_n^\alpha} |\{k \leq n : d(Z_k, Z_0) \geq \varepsilon\}|^\beta = 0$$

then the sequence $Z = (Z_k)$ is said to be ρ −statistically convergent of order (α, β) to Z_0 (or $S_\alpha^\beta(\rho, F)$ − convergent to Z_0, where ρ_n^α denotes the αth power of ρ_n , that is, $\rho^n = (\rho_n^\alpha) = (\rho_1^\alpha, \rho_2^\alpha, \ldots \rho_n^\alpha, \ldots)$. In this case, we write $S_\alpha^\beta(\rho, F) - \lim Z_k = Z_0$. $S_\alpha^\beta(\rho, F)$ will denote the set of all ρ −statistically convergent of order (α, β) for sequences of fuzzy numbers

Definition 3.2. Let $Z = (Z_k)$ be a sequence of fuzzy numbers, $0 < \alpha \leq \beta \leq 1$ and q is a positive real number. If there exists a fuzzy number Z_0 such that

$$\lim_{n\to\infty} \frac{1}{\rho_n^\alpha} \left(\sum_{k=1}^{n} [d(Z_k, Z_0)]^q \right)^\beta = 0$$

then the sequence $Z = (Z_k)$ is said to be strongly $w(\rho, F, q)$ −summable of order (α, β) to Z_0 (or strongly $w_\alpha^\beta(\rho, F, q)$ −summable). In this case, we write $w_\alpha^\beta(\rho, F, q) - \lim Z_k = Z_0$. $w_\alpha^\beta(\rho, F, q)$ will

denote the set of all strongly $w(\rho,F,q)$ −summable of order (α,β) for sequences of fuzzy numbers When $Z_0=\bar{0}$, we use $w_{\alpha,0}^{\beta}(\rho,F,q)$ instead of $w_{\alpha}^{\beta}(\rho,F,q)$.

Definition 3.3. Let f be a modulus function, $q=(q_k)$ be a sequence of positive real numbers, and $0<\alpha\leq\beta\leq 1$. If there exists a fuzzy number Z_0 such that

$$\lim_{n\to\infty}\frac{1}{\rho_n^{\alpha}}\left(\sum_{k=1}^{n}\left[f\left(d(Z_k,Z_0)\right)\right]^{q_k}\right)^{\beta}=0$$

then the sequence $Z=(Z_k)$ is said to be strongly $w(\rho,F,q,f)$ −summable of order (α,β) to Z_0 (or strongly $w_{\alpha}^{\beta}(\rho,F,q,f)$ −summable). In this case, we write $w_{\alpha}^{\beta}(\rho,F,q,f)-\lim Z_k=Z_0$. $w_{\alpha}^{\beta}(\rho,F,q,f)$ will denote the set of all strongly $w(\rho,F,q,f)$ −summable of order (α,β) for sequences of fuzzy numbers. When $Z_0=\bar{0}$, we use $w_{\alpha,0}^{\beta}(\rho,F,q,f)$ instead of $w_{\alpha}^{\beta}(\rho,F,q,f)$.

In the following theorems, we will assume that $q=(q_k)$ is a bounded sequence with $0<r=\inf_k q_k\leq q_k\leq\sup_k q_k=R<\infty$.

Theorem 3.1. Let $Z=(Z_k)$ be a sequence of fuzzy numbers, f be a modulus function and $\alpha_1,\alpha_2,\beta_1,\beta_2\in(0,1]$ be real numbers such that $0<\alpha_1\leq\alpha_2\leq\beta_1\leq\beta_2\leq 1$. In this case, we have $w_{\alpha_1}^{\beta_2}(\rho,F,q,f)\subset S_{\alpha_2}^{\beta_1}(\rho,F)$.

Proof. Let $Z\in w_{\alpha_1}^{\beta_2}(\rho,F,q,f)$ and $\varepsilon>0$ be given. Let the sums $\sum_1$ ve $\sum_2$ represent the sums over $k\leq n$, where $d(Z_k,Z_0)\geq\varepsilon$ and $d(Z_k,Z_0)<\varepsilon$ respectively. Since for every n, we have $\rho_n^{\alpha_1}\leq\rho_n^{\alpha_2}$,

$$\begin{aligned}\frac{1}{\rho_n^{\alpha_1}}\left(\sum_{k=1}^{n}\left[f\left(d(Z_k,Z_0)\right)\right]^{q_k}\right)^{\beta_2}&=\frac{1}{\rho_n^{\alpha_1}}\left(\sum_{1}\left[f\left(d(Z_k,Z_0)\right)\right]^{q_k}+\sum_{2}\left[f\left(d(Z_k,Z_0)\right)\right]^{q_k}\right)^{\beta_2}\\&\geq\frac{1}{\rho_n^{\alpha_2}}\left(\sum_{1}\left[f\left(d(Z_k,Z_0)\right)\right]^{q_k}+\sum_{2}\left[f\left(d(Z_k,Z_0)\right)\right]^{q_k}\right)^{\beta_2}\\&\geq\frac{1}{\rho_n^{\alpha_2}}\left(\sum_{1}[f(\varepsilon)]^{q_k}\right)^{\beta_2}\\&\geq\frac{1}{\rho_n^{\alpha_2}}\left(\sum_{1}\min\left([f(\varepsilon)]^{r},[f(\varepsilon)]^{R}\right)\right)^{\beta_2}\\&\geq\frac{1}{\rho_n^{\alpha_2}}|\{k\leq n:d(Z_k,Z_0)\geq\varepsilon\}|^{\beta_1}[\min\left([f(\varepsilon)]^{r},[f(\varepsilon)]^{R}\right])^{\beta_1}.\end{aligned}$$

Therefore $Z\in S_{\alpha_2}^{\beta_1}(\rho,F)$.

Theorem 3.2. Let $Z=(Z_k)$ be a sequence of fuzzy numbers, f be a bounded modulus function and $\lim_{n\to\infty}\frac{\rho_n^{\beta_2}}{\rho_n^{\alpha_1}}=1$. Then, $S_{\alpha_1}^{\beta_2}(\rho,F)\subset w_{\alpha_2}^{\beta_1}(\rho,F,q,f)$.

Proof. Let $Z\in S_{\alpha_1}^{\beta_2}(\rho,F)$, f is a bounded modulus function. Since f is bounded, there exists an integer M such that $f(x)\leq M$ for all x. For any $\varepsilon>0$, we can write:

$$\frac{1}{\rho_n^{\alpha_2}}\left(\sum_{k=1}^{n}\left[f\left(d(Z_k,Z_0)\right)\right]^{q_k}\right)^{\beta_1} \leq \frac{1}{\rho_n^{\alpha_1}}\left(\sum_{k=1}^{n}\left[f\left(d(Z_k,Z_0)\right)\right]^{q_k}\right)^{\beta_1}$$

$$= \frac{1}{\rho_n^{\alpha_1}}\left(\sum_{1}\left[f\left(d(Z_k,Z_0)\right)\right]^{q_k} + \sum_{2}\left[f\left(d(Z_k,Z_0)\right)\right]^{q_k}\right)^{\beta_1}$$

$$\leq \frac{1}{\rho_n^{\alpha_2}}\left(\sum_{1}\max\left(M^r, M^R\right) + \sum_{2}[f(\varepsilon)]^{q_k}\right)^{\beta_1}$$

$$\leq \left(\max\left(M^r, M^R\right)\right)^{\beta_2}\frac{1}{\rho_n^{\alpha_1}}|\{k \leq n: d(Z_k,Z_0) \geq \varepsilon\}|^{\beta_2}$$

$$+\frac{\rho_n^{\beta_2}}{\rho_n^{\alpha_1}}\left(\max\left(f(\varepsilon)^R, (f(\varepsilon)^R\right)\right)^{\beta_2}.$$

Thus, we can conclude that $Z \in w_{\alpha_2}^{\beta_1}(\rho, F, q, f)$.

Theorem 3.3. Let $Z = (Z_k)$ be a sequence of fuzzy numbers, f be a modulus function, $0 < \alpha \leq \beta \leq 1$ and $\liminf q_k > 0$. If the sequence $Z = (Z_k)$ is convergent to a fuzzy number Z_0, then the sequence $Z = (Z_k)$ is strongly $w(\rho, F, q, f)$ −summable of order (α, β).

Proof. Let $Z_k \to Z_0$. Since f is a modulus function, $f\left(d(Z_k,Z_0)\right) \to \bar{0}$. As $\liminf q_k > 0$, $\left[f\left(d(Z_k,Z_0)\right)\right]^{q_k} \to \bar{0}$. Thus, we have $w_\alpha^\beta(\rho, F, q, f) - \lim Z_k = Z_0$. This is what we wanted to prove.

Theorem 3.4. Let $Z = (Z_k)$ be a sequence of fuzzy numbers, f be a modulus function, $0 < \alpha = \beta \leq 1$, $q > 1$ and $\lim\limits_{u\to\infty}\inf \frac{f(u)}{u} > 0$. Then $w_\alpha^\beta(\rho, F, q, f) \subset w_\alpha^\beta(\rho, F, q)$.

Proof. When $\lim\limits_{u\to\infty}\inf \frac{f(u)}{u} > 0$ for $u > 0$, it means that there exists a positive number c such that $f(u) > cu$ holds $u > 0$. Let $Z \in w_\alpha^\beta(\rho, F, q, f)$. Therefore, we have

$$\frac{1}{\rho_n^\alpha}\left(\sum_{k=1}^{n}\left[f\left(d(Z_k,Z_0)\right)\right]^{q}\right)^{\beta} \geq \frac{1}{\rho_n^\alpha}\left(\sum_{k=1}^{n}[cd(Z_k,Z_0)]^{q}\right)^{\beta} = \frac{c^{q\beta}}{\rho_n^\alpha}\left(\sum_{k=1}^{n}[d(Z_k,Z_0)]^{q}\right)^{\beta}.$$

Consequently, we have obtained $w_\alpha^\beta(\rho, F, q, f) \subset w_\alpha^\beta(\rho, F, q)$.

Theorem 3.5. Let $Z = (Z_k)$ be a sequence of fuzzy numbers, f be a modulus function and $\lim q_k > 0$. If the sequence $Z = (Z_k)$ is strongly $w_\alpha^\beta(\rho, F, q, f)$ −summable to the fuzzy number Z_0, then the limit is unique.

Proof. Let $w_\alpha^\beta(\rho, F, q, f) - \lim Z_k = Z_0$, $w_\alpha^\beta(\rho, F, q, f) - \lim Z_k = Z_0'$ and $\lim q_k = t > 0$. In this case, we can obtain the following:

$$\lim_{n\to\infty}\frac{1}{\rho_n^\alpha}\left(\sum_{k=1}^{n}\left[f\left(d(Z_k,Z_0)\right)\right]^{q_k}\right)^{\beta} = 0$$

and

$$\lim_{n\to\infty}\frac{1}{\rho_n^{\alpha}}\left(\sum_{k=1}^{n}\left[f\left(d(Z_k,Z_0')\right)\right]^{q_k}\right)^{\beta}=0.$$

Thus, from the definition of f and (1), for $\sup_k q_k = K$, $0<\alpha\leq\beta\leq 1$ ve $N=\max(1,2^{K-1})$, we can write:

$$\frac{1}{\rho_n^{\alpha}}\left(\sum_{k=1}^{n}\left[f\left(d(Z_0,Z_0')\right)\right]^{q_k}\right)^{\beta}\leq\frac{N}{\rho_n^{\alpha}}\left(\sum_{k=1}^{n}\left[f\left(d(Z_k,Z_0)\right)\right]^{q_k}+\sum_{k=1}^{n}\left[f\left(d(Z_k,Z_0')\right)\right]^{q_k}\right)^{\beta}$$
$$\leq\frac{N}{\rho_n^{\alpha}}\left(\sum_{k=1}^{n}\left[f\left(d(Z_k,Z_0)\right)\right]^{q_k}\right)^{\beta}+\frac{N}{\rho_n^{\alpha}}\left(\sum_{k=1}^{n}\left[f\left(d(Z_k,Z_0')\right)\right]^{q_k}\right)^{\beta}.$$

Therefore, we have:

$$\frac{1}{\rho_n^{\alpha}}\left(\sum_{k=1}^{n}\left[f\left(d(Z_0,Z_0')\right)\right]^{q_k}\right)^{\beta}=0.$$

Since $\lim q_k = t$, we can conclude that $Z_0 - Z_0' = 0$. Thus, the limit is unique.

Theorem 3.6. Let $Z=(Z_k)$ be a sequence of fuzzy numbers, f be a modulus function and $0<\alpha_1\leq\alpha_2\leq\beta_1\leq\beta_2\leq 1$. Let $\rho=(\rho_n)$ and $\tau=(\tau_n)$ be two sequences such that $\rho_n\leq\tau_n$ for every $n\in\mathbb{N}$. In this case:

(i) If $\liminf_{n\to\infty}\frac{\rho_n^{\alpha_1}}{\tau_n^{\alpha_2}}>0$, then $w_{\alpha_2}^{\beta_2}(\tau,F,q,f)\subset w_{\alpha_1}^{\beta_1}(\rho,F,q,f)$. (2)

(ii) If $\limsup_{n\to\infty}\frac{\rho_n^{\alpha_1}}{\tau_n^{\alpha_2}}<\infty$, then $w_{\alpha_1}^{\beta_2}(\rho,F,q,f)\subset w_{\alpha_2}^{\beta_1}(\tau,F,q,f)$. (3)

Proof. (i) Let $Z=(Z_k)\in w_{\alpha_2}^{\beta_2}(\tau,F,q,f)$ be a sequence of fuzzy numbers satisfying (2). In this case:

$$\frac{1}{\tau_n^{\alpha_2}}\left(\sum_{k=1}^{n}\left[f\left(d(Z_k,Z_0)\right)\right]^{q_k}\right)^{\beta_2}\geq\frac{\rho_n^{\alpha_1}}{\tau_n^{\alpha_2}}\frac{1}{\rho_n^{\alpha_1}}\left(\sum_{k=1}^{n}\left[f\left(d(Z_k,Z_0)\right)\right]^{q_k}\right)^{\beta_1}$$

Thus, if $Z\in w_{\alpha_2}^{\beta_2}(\tau,F,q,f)$, then $Z\in w_{\alpha_1}^{\beta_1}(\rho,F,q,f)$.

(ii) Let $Z=(Z_k)\in w_{\alpha_1}^{\beta_2}(\rho,F,q,f)$ and (3) holds. In this case, since $\rho_n\leq\tau_n$ for every $n\in\mathbb{N}$:

$$\frac{1}{\tau_n^{\alpha_2}}\left(\sum_{k=1}^{n}\left[f\left(d(Z_k,Z_0)\right)\right]^{q_k}\right)^{\beta_1}\leq\frac{1}{\tau_n^{\alpha_2}}\left(\sum_{k=1}^{n}\left[f\left(d(Z_k,Z_0)\right)\right]^{q_k}\right)^{\beta_2}=\frac{\rho_n^{\alpha_1}}{\tau_n^{\alpha_2}}\frac{1}{\rho_n^{\alpha_1}}\left(\sum_{k=1}^{n}\left[f\left(d(Z_k,Z_0)\right)\right]^{q_k}\right)^{\beta_2}.$$

Therefore, $w_{\alpha_1}^{\beta_2}(\rho,F,q,f)\subset w_{\alpha_2}^{\beta_1}(\tau,F,q,f)$.

Ethical statement:

The author declares that this document does not require ethics committee approval or any special permission. Our study does not cause any harm to the environment.

Conflict of interest:

The author declares no potential conflicts of interest related to this article's research, authorship, and publication.

References

[1] Fast, H., "Sur la convergence statistique", *Colloquium Math*., 2, 241-244, 1951.

[2] Steinhaus, H., "Sur la convergence ordinaire et la convergence asymptotique*", Colloq. Math*. 2, 73-74, 1951.

[3] Schoenberg, I.J., "The Integrability of Certain Functions and Related Summability Methods", *Amer. Math. Monthly*, 66, 361-375, 1959.

[4] Aral, N. D., & Et, M., "Generalized difference sequence spaces of fractional order defined by Orlicz functions", *Communications Faculty of Sciences University of Ankara Series A1 Mathematics and Statistics* , 69 (1) , 941-951, 2020.

[5] Aral, N.D., & Gunal, S., "On $\boldsymbol{M}_{\boldsymbol{\lambda}_{m,n}}$statistical convergence", *Journal of Mathematics*, 1–8, 2020.

[6] Aral, N.D., & Kandemir, H. Ş., "$\boldsymbol{I}$ −lacunary statistical convergence of order $\boldsymbol{\beta}$ of difference sequences of fractional order", *Facta Univ. Ser. Math. Inform.* 36 (1), 43—55, 2021.

[7] Şengül, H., Et, M., & Altin, Y., "f-lacunary statistical convergence and strong f-lacunary summability of order $\boldsymbol{\alpha}$ of double sequences", *Facta Univ. Ser. Math. Inform.* 35 (2), 495—506, 2020.

[8] Zadeh, L. A., "Fuzzy sets", *Inform and Control*, 8, 338-353, 1965.

[9] Matloka, M., "Sequences of fuzzy numbers", *BUSEFAL*, 28, 28-37, 1986.

[10] Nuray, F., Savaş, E., "Statistical convergence of sequences of fuzzy real numbers", *Math. Slovaca* 45(3), 269-273, 1995.

[11] Kwon, J.S., "On statistical and p-Cesaro Convergence of fuzzy numbers", *Korean J. Comput. & Appl. Math.*, 7(1), 195-203, 2000.

[12] Gadjiev, A.D., Orhan, C., "Some approximation theorems via statistical convergence", *Rocky Mt J Math.* 32(1),129–138, 2002.

[13] Çolak, R., "Statistical convergence of order α. Modern methods in analysis and its applications", *Anamaya Pub, New Delhi*, 121–129, 2010.

[14] Şengül, H., "Some Cesàro-type summability spaces defined by a modulus function of order $(\boldsymbol{\alpha}, \boldsymbol{\beta})$", *Commun. Fac. Sci. Univ. Ank. Sér. A1 Math. Stat.* 66(2), 80—90, 2017.

[15] Altınok, H., & Et, M., "Statistical convergence of order $(\boldsymbol{\beta}, \boldsymbol{\gamma})$ for sequences of fuzzy numbers", *Soft Computing*, 23, 6017-6022, 2019. doi:10.1007/s00500-018-3569-z

[16] Çakallı, H., "A variation on statistical ward continuity", *Bull. Malays. Math. Sci. Soc*. 40, 1701-1710, 2017. doi:10.1007/s40840-015-0195-0

[17] Aral., N.D., "ρ-statistical convergence defined by modulus function of order (α, β)", *Maltepe Journal of Mathematics*, 4(1), 15-23, 2022. doi:10.47087/mjm.1092599

[18] Kandemir, H.Ş., "On ρ-statistical convergence in topological groups*", Maltepe Journal of Mathematics*, 4(1), 9-14, 2022. doi:10.47087/mjm.1092559

[19] Aral, N.D., Kandemir, H.Ş., Et. M., "On **ρ**− Statistical convergence of sequences of Sets", *Conference Proceeding Science and Tecnology*, 3(1),156-159, 2020.

[20] Gumus, H., "Rho-statistical convergence of interval numbers", International Conference on Mathematics and Its Applications in Science and Engineering. 2022.

[21] Aral, N.D., Kandemir, H., & Et, M., "On ρ−statistical convergence of order α of sequences of function", *e-Journal of Analysis and Applied Mathematics,* 2022(1), 45-55, 2022.

[22] Cakalli, H., Et, M., & Şengül, H., "A variation on $\boldsymbol{N_\theta}$ − ward continuity", *Georgian Math. J.* 27 (2), 191—197, 2020.

[23] Nakano, H., "Concave modular", *J. Math. Soc. Japan*, 5, 29-49.

[24] Maddox, I.J., "Spaces of strongly summable sequences", *The Quarterly Journal of Mathematics*, 18(1), 345-355, 1967.

Middle East Journal of Science

https://dergipark.org.tr/mejs **MEJS**

e-ISSN:2618-6136

Research Article

SPERM PARAMETERS' PREDICTIVE VALUE IN INTRAUTERINE INSEMINATION SUCCESS: A SINGLE-CENTER EXPERIENCE

Muhamet AFSİN*[1] Ayse Feyda NURSAL[2] Serap Mutlu ÖZCELİK OTCU[3] Dilek YAVUZ[1] Serhat EGE[4]

[1]Dep. of Andrology, Health Sciences University, Gazi Yasargil Edu. and Research Hospital, Diyarbakir, Turkiye
[2]Department of Medical Genetics, Hitit University, Faculty of Medicine, Corum, Turkiye
[3]Dep. of Obstetrics and Gynecology, Health Sci. Uni., Gazi Yasargil Edu. and Res. Hos., Diyarbakir, Turkiye
[4]Department of Obstetrics and Gynecology, Dicle University, Faculty of Medicine, Diyarbakir, Turkiye
* Corresponding author; afsin.muhammet21@hotmail.com

Abstract: *Although intrauterine insemination is a widely used assisted reproductive technique no consensus on sperm parameters affects the probability of pregnancy. Therefore, the purpose of this study was to determine whether semen parameters affect intrauterine insemination (IUI) success. A total of 403 couples (345 negative pregnancies, and 58 positive pregnancies) that underwent 549 intrauterine insemination treatment cycles for heterogenous indications were included in the study. Clomiphene citrate, letrazole, and/or gonadotropins were used for ovarian stimulation in women in this study. The spermiogram tests of the spouse receiving IUI treatment were examined. Clinical pregnancy occurred in 58 of 549 intrauterine insemination (10.56%). Unexplained infertility, polycystic ovary syndrome, and cervical-tubal factors were higher in the positive pregnancy group compared to the negative pregnancy group while the malefactor was more prevalent in the negative pregnancy group compared to the positive pregnancy group (p=0.03). There was no statistical difference between women with positive and negative pregnancies in terms of age (≤ 35 and > 35), body mass index, infertility type, infertility time, endometrial thickness on HCG day, stimulation protocol, cycle numbers, number of insemination, estradiol, prolactin, LH, FSH, and TSH levels (p>0.05). The sperm characteristics in males [ejaculate volume, sperm concentration, total sperm count, motility, immotility, and total progressively motile sperm count] did not significantly differ between positive and negative pregnancy groups (p>0.05). The present study found that the conception probability of intrauterine insemination did not correlate with the spectrogram parameters.*

Keywords*: İntrauterine insemination, infertility, sperm parameters.*

Received: September 28, 2023 *Accepted: December 25, 2023*

1. Introduction

Infertility means the inability to conceive after regular intercourse for one year without contraceptives. 10-15 % of the couples are not fertile [1]. Intrauterine insemination (IUI) is the first-line treatment, a cost-effective and noninvasive procedure for treating infertile couples. This treatment is done by inserting a higher concentration of the made sperms into the uterine cavity. Infertile couples have used this technique for many years to treat fertility [2]. They are using the IUI technique combined with controlled ovarian stimulation led to higher hope for infertile couples' pregnancy. For unexplained infertility, it has been reported that the pregnancy rate with IUI has been 9 to 20% [3,4].

Many factors have played a potential role in predicting and optimizing the success of IUI, including duration and type of infertility, endometrial thickness, number of mature follicles, and different seminal parameters.

The first step is a semen analysis is to diagnose male infertility accurately. According to the WHO's guidelines, the volume, concentration, abnormal and normal morphology, viscosity, and motility of spermatozoa are described by standard semen quality assessment [5]. The *sperm morphology using strict criteria, * Total motile sperm count (TMSC), and * Number of motile spermatozoa inseminated (NMSI) are the most frequently examined sperm parameters concerning pregnancy rates in the native sperm sample [6]. Total motility is the most common parameter in the native sperm sample. According to a systematic review, a morphology > 4% and a TMSC > 1 million are of possible prognostic value. In such a case, IUI should be withheld below these cut-off levels [6]. However, the evidence quality was low. The focus of the previous studies has been on the effect of follicle size and hormonal stimulation on the assisted reproduction techniques (ART) outcome and IUI outcome. Bensdorp et al. found a cumulative pregnancy rate of 47% after six IUI cycles with controlled ovarian hyperstimulation in twelve months [7].

Although IUI is a widely used ART, no consensus on sperm parameters affects the probability of pregnancy. Therefore, this study aimed to determine whether semen parameters affect IUI success.

2. Materials and Methods

2.1. Study population

In this study, 549 cycles of 403 infertile patients who underwent IUI after ovulation induction in the Infertility clinic of the Gazi Yasargil Education and Research Hospital, between January and May 2021 were examined. The couples suspected of primary or secondary infertility for 1 year or more and could not achieve spontaneous pregnancy were examined in this study. All participants were aged 40 years and below. Couples with below 1 year of marriage, over 40 years, and men with severe oligozoospermia-azoospermia were excluded from the study. All female patients underwent ovarian stimulation with human gonadotropin (HCG), clomiphene, or letrozole, or a combination of clomiphene or letrozole and HCG (8-10). Body mass index (BMI), estradiol (E2), prolactin, luteinizing hormone (LH), follicle-stimulating hormone (FSH), and thyroid-stimulating hormone (TSH) values were obtained from their files. Hormone analyses of all female patients were performed on the 3rd day of the menstrual period. The spirogram tests of the spouse receiving IUI treatment were examined.

Ethical Statement: The study was approved by Health Sciences University, Ethics Committee. (date and number of approval: 2021/858). This study was carried out according to the current Helsinki Declaration.

2.2. Semen analysis

Sperm samples were collected from the participants who were sexually abstinent for 2-7 days by masturbating into sterile disposable plastic cups without using any lubricant. Semen samples taken from the participants were examined in conformity with World Health Organization (WHO) criteria after liquefaction. The semen samples were first homogenized by pipetting with a Pasteur pipette. Approximately 10 µl of semen was pipetted and placed on the Makler camera (counting chamber) and sealed with a glass lid to determine the count and motility. Spermatozoa in 10 squares were counted through the x20 lens of the light microscope (Olympus CX31), and the result was expressed in millions. It was evaluated that sperm parameters including viscosity, leucocyte count, sperm

concentration, total sperm count, motility, immotilty, and total progressive motile sperm count (TPMSC).

2.3. Semen Preparation with the Density Gradient Separation

The density gradient separation removes seminal fluid and improves sperm quality for IUI. A 2-layer gradient was prepared using approximately 1.0 ml of each 45%-90% gradient in a conical tube. In a conical centrifuge tube, semen was layered onto the gradient and then centrifuged at 1800 rpm for 15 minutes. After the supernatant was removed, an additional 2-3 ml of washing medium was placed on it, and it was centrifuged again at 1800 rpm for 10 minutes. The upper part of the tubes was discarded again, and 0.5 ml of washing medium was added to the lower 0.5-1 ml part. It was withdrawn into the catheter and ready for intrauterine administration.

2.4. Statistical analysis

SPSS 21.0 (IBM SPSS Inc., Armonk, NY, USA) was used for statistical analysis. The normality of data distribution was tested with the Shapiro-Wilk test. When the data did not fit the normal distribution, Mann-Whitney U and Wilcoxon tests were used for pairwise comparison. Data were defined as mean and standard deviation. Student's t-test and Chi-Square test were used for statistical analysis to see whether there was a significant difference between the means of positive and negative pregnancy data. $p \leq 0.05$ was considered significant.

3. Results

A total of 403 couples (345 negative pregnancies, and 58 positive pregnancies) that underwent 549 IUI treatment cycles for heterogenous indications were included in the study. Clinical pregnancy occurred in 58 of 549 IUI (10.56%). There was a significant difference between women with positive and negative pregnancies in the causes of infertility. Unexplained infertility, polycystic ovary syndrome (PCOS), and cervical-tubal factors were higher in the positive pregnancy group than in the negative pregnancy group ($p=0.03$). Also, the malefactor was more prevalent in women with negative pregnancies than in the group with positive pregnancies. There was no statistical difference between women with positive and negative pregnancies in terms of age (≤ 35 and > 35), BMI, infertility type, infertility time, endometrial thickness on HCG day, stimulation protocol, cycle numbers, number of insemination, FSH, LH, E2, prolactin and TSH levels ($p>0.05$). Demographic and clinical findings of women who underwent IUI in the study are given in Table 1.

Table 1. Demographical and clinical characteristics of women who underwent IUI

Characteristics	**Positive pregnancy** (n: 58) (%)	**Negative pregnancy** (n: 345) (%)	**p**
Woman's age (years),			
≤ 35 n %	49 (84.5)	272 (78.8)	
> 35 n %	9 (15.5)	73 (21.2)	0.308
BMI (kg/m²)			
≤ 18.5, n (%)	2 (3.5)	7 (2.1)	
18.5 – 24.9, n (%)	27 (46.5)	167 (48.4)	0.757
25.0 – 29.9, n (%)	18 (31)	123 (35.6)	
≥ 30, n (%)	11 (19)	48 (13.9)	
Infertility type			
Primary infertility, n (%)	38 (65.5)	218 (63.2)	
Secondary infertility, n (%)	20 (34.5)	127 (36.8)	0.811
Cause of infertility			
Male factor, n (%)	5 (8.6)	88 (25.5)	0.03
Unexplained infertility, n (%)	46 (79.3)	234 (67.8)	
PCOS, n (%)	2 (3.5)	6 (1.7)	
Cervical-tubal factors, n (%)	4 (6.9)	10 (2.8)	
Low ovary reserve, n (%)	1 (1.8)	7 (2)	
Endometrial thickness on HCG day			
≤ 8 mm, n (%)	37 (63.8)	230 (66.7)	0.68
> 8 mm, n (%)	21 (36.2)	115 (33.3)	
Number of dominant follicles of day on HCG			
1	40 (68.9)	244 (70.7)	0.5
2	18 (31.1)	101 (29.3)	
Stimulation protocol			
CC (only), n (%)	10 (17.3)	66 (19.1)	0.7
Letrazole (only), n (%)	24 (41.4)	126 (36.5)	
CC + Letrazole, n (%)	8 (13.8)	47 (13.6)	
Gonodotropines (only), n (%)	13 (22.4)	96 (27.9)	
Letrazole + Gonodotropin, n (%)	3 (5.1)	10 (2.9)	
Infertility period, years, mean ± SD	3.13 ± 2.35	3.34 ± 2.62	0. 847
Cycle numbers, mean ± SD	2.94 ± 1.60	3.43 ± 2.07	0.126
Number of insemination, mean ± SD	1.25± 0.36	1.41 ± 0.64	0.534
FSH (IU/L)			
≤ 8, n (%)	53 (91.4)	287 (83.2)	0.119
> 8, n (%)	5 (8.6)	58 (16.7)	
LH (IU/L), mean ± SD	5.84 ± 3.30	7.00 ± 5.48	0,098
E2 (pg/mL), mean ± SD	39.30 ±18.14	37.36 ± 24.13	0.599
Prolactin (µg/L), mean ± SD	16.23 ± 9.06	14.63 ± 9.19	0.395
TSH (mU/L), mean ± SD	1.72 ± 0.86	1.73 ± 1.02	0.69

BMI: Body Mass Index; CC: Clomiphen Citrate; E2: Estradiol; FSH: Folıcule Stimulating Hormone; HCG: Human Corıonic Gonadotropin; LH: Luteinizing Hormone; PCOS: Poly Cystic Ovary Syndrome; SD: Standart Deviation; TSH: Thyroid Stimulating Hormone.

Then, we examined the demographic features and sperm characteristics of the males of positive and negative pregnancy groups. The demographic and sperm characteristics(ejaculate volum, sperm concentration, total sperm count, motility, immotility, and TPMSC) in males did not significantly differ between positive and negative pregnancy groups (*p>0.05*). The results of demographic characteristics and sperm parameters are presented in Table 2.

Table 2. Comparison of demographic characteristics and sperm parameters in the partners with pregnancy (+) and pregnancy (-) women undergoing IUI

Characteristics	**Positive pregnancy** (n: 58) (%)	**Negative pregnancy** (n: 345) (%)	**p**
Age (years),			
≤ 35, n (%)	41 (70.7)	234 (67.8)	0.717
> 35, n (%)	17 (29.3)	111 (32.2)	
Abstinence period (day), mean ± SD	3.07 ± 0.29	3 ± 0.35	0.232
Ejaculate volum (ml), mean ± SD	2.61 ± 1.04	2.95 ± 2.16	0.194
Sperm concentration (million/ml), mean ± SD	56.39 ±39.03	50.65 ± 38.78	0.29
≤ 15, n (%)	6 (10.3)	67 (19.5)	
15-90, n (%)	41 (70.7)	238 (68.9)	0.18
≥ 90, n (%)	11 (19)	40 (11.6)	
Total sperm count (million), mean ± SD	149.69 ± 122.49	140.31 ± 113.65	0.56
≤ 39, n (%)	7 (12,1)	75 (21,7)	0.09
> 39, n (%)	51 (87,9)	270 (78,3)	
Motility (%)			
Progressive (%), mean ± SD	48.05 ± 17.34	52.12 ± 17.73	0.1
≤ 32, n (%)	12 (20.7)	50 (14.5)	0.2
> 32, n (%)	46 (79.3)	295 (85.5)	
Non progressive (%), mean ± SD	8.9 ± 4.6	8.1 ± 5.5	0.31
Immotility (n,%), mean ± SD	42.8 ± 16.56	39.74 ± 16.76	0.19
TPMSC (million), mean ± SD	75.90 ± 79.00	77. 0 ± 70.55	0.99
≤ 30, n (%)	14 (24.2)	121 (35)	0.13
> 30, n (%)	44 (75.8)	224 (65)	

SD: Standart Deviation; TPMSC: Total Progressive Motile Sperm Count

4. Discussion

Although there were revolutionary advances in assisted reproduction, such as intracytoplasmic sperm injection (ICSI), in vitro fertilization (IVF), IUI, and subzonal insemination (SUZI), it remains a noninvasive, inexpensive, and effective first-line therapy for the selected patients with moderate male factor, cervical factor, immunological infertility, unexplained infertility, and infertility because of ejaculatory disorders. It is also suggested as a therapy for ovarian dysfunction, endometriosis, and even tubal factors [11]. Now, male factor infertility is increasing, and the clinical diagnosis is only based on semen parameters. A few studies have only evaluated the predictive value of the WHO criteria for infertile couples' semen [12,13]. Based on the previous studies, a criterion for choosing between IVF and IUI was the total number of motile spermatozoa of semen, suggesting the threshold values of 5-10 million [14]. However, Van Voorhis et al., Akanji et al., and Dorjpurev et al. suggested that IUI is possible when TMSC is more than 10 million. It was also found that motile sperm inseminated ≥ 10 million and normal sperm morphology ≥ 5% are useful prognostic factors of IUI cycles [15-17]. In addition, it was reported that normal sperm morphology ≥ 5% and motile sperm

inseminated ≥ 10 million are useful markers for IUI [18]. However, some studies consider the number of motile sperm counts over one million as an important predictive parameter in IUI [6,19]. According to the publication based on a longitudinal cohort study, the prewash TMSC better correlated with the ongoing pregnancy rate of natural conception than the classification by WHO 2010 [20]. Also, Ates et al. found a correlation between initial progressive motile sperm count and sperm count after washing [21]. According to Yalti's report, the TMSC, percent, and motility of fast motile sperm were the independent predictors of successful IUI [22]. In a study in Turkey, it was found that there was no statistically significant difference between the TPMSC ≤ 10 million and TPMSC >10 million groups and between the morphology ≤ 4% and morphology > 4% groups in terms of clinical pregnancy rates [23]. Irrespective of this, there is still no sufficient evidence concluding that IUI affects the mild male factor infertility [24]. The reports published have been arguable in this field. Several studies found no association between sperm and outcome count after IUI. It was declared that none of the sperm parameters predicted the pregnancy after the first IUI cycle [25]. In an analysis evaluating 20 observational studies, it was reported that there is no clinical difference between those normal and abnormal sperm morphologies in IUI pregnancy success when total motile sperm count and female age are taken into account [26].

Therefore, we aimed to analyze the influence of semen parameters, including sperm concentration, total sperm count, motility, immotility, and TPMSC, on the IUI results. In our study, we evaluated the data of 403 couples as a single center. In the present study, 58 positive pregnancies were achieved from 549 IUI cycles, resulting in a 10.56% rate. Our results are in line with other data. We also examined the features of the women participating in the study. In this evaluation, the cause of infertility in women showed a different distribution in a positive and negative pregnancy. The malefactor was more prevalent in the negative pregnancy group than the positive pregnancy group, while PCOS and cervical-tubal factors were higher in the positive pregnancy group than the negative pregnancy group (Table 1) There was no significant relationship between spectrogram parameters ejaculate volume, sperm concentration, total sperm count, motility, immotility, and TPMSC) and the probability of pregnancy in women who underwent IUI (Table 2).

This study has some limitations. Our study was conducted in a single center and was a heterogeneous group. However, the number of participants was crowded. Another important limitation of our study is that the sperm morphology of these patients could not be examined. It can also be considered an advantage to evaluate many parameters.

5. Conclusion

The present study found that the conception probability of IUI did not correlate with the spectrogram parameters. The current results should be cautiously interpreted, which should be confirmed by further research with advanced study analysis and design.

Ethical Statement:

The study was approved by the Health Sciences University Ethics Committee. (date and number of approval: 2021/858).

Informed Consent:

Written informed consent was obtained from subjects and patients who participated in this study.

Conflict of Interest:

The authors declared no conflicts of interest concerning the authorship and/or publication of this article.

Financial Disclosure:

The authors declared that this study has received no financial support.

Author Contributions:

M.A.; A.F.N: Writing - Original draft preparation
M.A, D.Y, S.E., S.M.O: Methodology
M.A.; A.F.N: Formal analysis, Writing
M.A, D.Y, S.E., S.M.O: Conceptualization, Methodology
M.A.: Investigation
A.F.N: Resources
All authors read and approved the final manuscript.

References

[1] De Sutter, P., ''Rational diagnosis and treatment in infertility'', *Best Practice Res Clin Obstet Gynaecol*, 20, 647-4, 2006. https://doi.org/10.1016/j.bpobgyn.2006.04.005.

[2] Hum ESHRE, Capri Workshop Group. Intrauterine insemination. ESHRE Capri Workshop Group. Intrauterine insemination. *Hum Reprod Update*, 15, 265-77, 2009. https://doi.org/10.1093/humupd/dmp003.

[3] Stone, B.A., Vargyas, J.M., Ringler, G.E., Stein, A.L., Marrs, R.P., ''Determinants of the outcome of intrauterine insemination: analysis of outcomes of 9963 consecutive cycles'' *Am J Obstet Gynecol*, 180(6 Pt 1), 1522-34, 1999. https://doi.org/10.1016/S0002-9378(99)70048-7.

[4] van der Westerlaken, L.A., Naaktgeboren, N., Helmerhorst, F.M., ''Evaluation of pregnancy rates after intrauterine insemination according to indication, age, and sperm parameters'', *J Assist Reprod Genet*,15, 359-64, 1998.

[5] World Health Organization., ''WHO laboratory manual for the examination of human semen and sperm-cervical mucus interaction. 5th ed. Cambridge'', Cambridge University 2010.

[6] Ombelet, W., Dhont, N., Thijssen, A., Bosmans, E., Kruger, T., ''Semen quality and prediction of IUI success in male subfertility: a systematic review'', *Reprod Biomed Online*, 28, 300-9, 2014. https://doi.org/10.1016/j.rbmo.2013.10.023.

[7] Bensdorp, A.J., et al., ''Prevention of multiple pregnancies in couples with unexplained or mild male subfertility: randomised controlled trial of in vitro fertilisation with single embryo transfer or in vitro fertilisation in the modified natural cycle compared with intrauterine insemination with controlled ovarian hyperstimulation'', *BMJ*, 350, g7771, 2015. DOI: 10.1136/bmj.g7771. doi: https://doi.org/10.1136/bmj.g7771

[8] Sakar, M.N., Oglak, S.C., ''Letrozole is superior to clomiphene citrate in ovulation induction in patients with polycystic ovary syndrome'', *J Med Sci*, 36(7), 1460-1465, 2020. doi: https://doi.org/10.12669/pjms.36.7.3345.

[9] Oğlak, S.C., Sakar, M.N., Ege, S., "Comparison of the efficacy of letrozole and gonadotropin combination versus gonadotropin alone in intrauterine insemination cycles in patients with unexplained infertility", *Eastern J Med,* 25(3), 427-433, 2020. DOI: 10.5505/ejm.2020.24993.

[10] Sakar, M.N., Oğlak, S.C., ''Comparison of the efficacy of letrozole stair-step protocol with clomiphene citrate stair-step protocol in the management of clomiphene citrate-resistant polycystic ovary syndrome patients'', *J Obstet Gynaecol Res*, 47(11), 3875-3882, 2021. https://doi.org/10.1111/jog.14936.

[11] Allahbadia, G.N., ‘’Intrauterine Insemination: Fundamentals’’ *Revisited.J Obstet Gynaecol India*, 67: 385-92, 2017. DOI 10.1007/s13224-017-1060-x.

[12] Deveneau, N.E., et al., ‘’Impact of sperm morphology on the likelihood of pregnancy after intrauterine insemination’’, *Fertil Steri*l, 102, 1584-90, 2014. https://doi.org/10.1016/j.fertnstert.2014.09.016.

[13] Mankus, E.B., et al., ‘’Prewash total motile count is a poor predictor of live birth in intrauterine insemination cycles’’ Fertil Steril, 111, 708-13, 2019. https://doi.org/10.1016/j.fertnstert.2018.12.025

[14] Miller, D.C., et al., ‘’Processed total motile sperm count correlates with pregnancy outcome after intrauterine insemination’’ Urology, 60, 497-501, 2002. https://doi.org/10.1016/S0090-4295(02)01773-9

[15] Van Voorhis, B.J., Barnett, M., Sparks, A.E., Syrop, C.H., Rosenthal, G., Dawson, J., ‘’Effect of the total motile sperm count on the efficacy and cost-effectiveness of intrauterine insemination and in vitro fertilization’’ Fertil Steril, 75, 661-68, 2001. https://doi.org/10.1016/S0015-0282(00)01783-0

[16] Akanji Tijani, H., Bhattacharya, S., ‘’The role of intrauterine insemination in male infertility’’, *Hum Fertil (Camb)*, 13, 226-32, 2010. https://doi.org/10.3109/14647273.2010.533811.

[17] Dorjpurev, U., et al., ‘’Effect of semen characteristics on pregnancy rate following intrauterine insemination'', *J Med Invest*, 58, 127-33, 2011. https://doi.org/10.2152/jmi.58.127

[18] Nikbakht, R., Saharkhiz, N., ‘’The influence of sperm morphology, total motile sperm count of semen and the number of motile sperm inseminated in sperm samples on the success of intrauterine insemination’’, *Int J Fertil Steril*, 5, 168-73, 2011.

[19] Merviel, P., Heraud, M.H., Grenier, N., Lourdel, E., Sanguinet, P., Copin, H., ‘’Predictive factors for pregnancy after intrauterine insemination (IUI): an analysis of 1038 cycles and a review of the literature’’ Fertil Steril, 93, 79-88, 2010. https://doi.org/10.1016/j.fertnstert.2008.09.058.

[20] Hamilton, J.A., et al., ‘’Total motile sperm count: a better indicator for the severity of male factor infertility than the WHO sperm classification system’’, *Hum Reprod*, 30, 1110-21, 2015. doi:10.1093/humrep/dev058.

[21] Ates, E., Akdag, A., Kol, A., Turan, O.D., Erol, H., ‘’Intrauterine insemination experience of a university hospital: Pregnancy rate and associated factors’’, Androl Bul, 23(2), 82-86, 2021. https://doi.org/10.24898/tandro.2021.85619.

[22] Yalti, S., Gürbüz, B., Sezer, H., Celik, S., ‘’Effects of semen characteristics on IUI combined with mild ovarian stimulation’’, Arch Androl, 50, 239-246, 2004. https://doi.org/10.1080/01485010490448435.

[23] Tasın, C., Ozaksit, G., ‘’The relationship between sperm parameters and pregnancy outcomes in patients with intrauterine insemination’’, *Türk Kadın Sağlığı ve Neonatoloji Dergisi*, 3(3), 60-66. 2021. DOI: 10.46969/ezh.962608.

[24] Bensdorp, A.J., Cohlen, B.J., Heineman, M.J., Vandekerckhove, P., ‘’Intra-uterine insemination for male subfertility’’ *Cochrane Database Syst Rev*, (3), CD000360, 2007. https://doi.org/10.1002/14651858.CD000360.

[25] Lemmens, L., et al., ‘’Semen Section of the Dutch Foundation for Quality Assessment in Medical Predictive value of sperm morphology and progressively motile sperm count for pregnancy outcomes in intrauterine insemination’’, *Fertil Steril*, 105, 1462-68, 2016. https://doi.org/10.1016/j.fertnstert.2016.02.012.

[26] Kohn, T.P., Kohn, J.R., Ramasamy, R., ‘’Effect of Sperm Morphology on Pregnancy Success via Intrauterine Insemination’’, *A Systematic Review and Meta-Analysis. J Urol*, 199, 812-22, 2018. https://doi.org/10.1016/j.juro.2017.11.045